Synchronization under Hardware Impairments in Over-6GHz Wireless Industrial IoT Systems

Kapseok Chang, Woncheol Cho, Byung-Jae Kwak, and Young-Jo Ko

Abstract—Mobile devices perform cell search for initial access in cellular-based industrial Internet of Things (IoT) systems. Existing fifth-generation (5G) New Radio (NR) cell-search scheme provides timing synchronization and cell identification. Usage scenarios emerging with the growth of the IoT market require unprecedented precision, reliability, and scalability in the future network, and a shift toward high frequency bands can be one of the key enablers to achieve these stringent requirements. However, in high frequency bands, hardware impairments including carrier frequency offset and phase noise are exacerbated, and a sharp beam causes the problem of cell identity (ID) ambiguity that can reach further than a reduced cell coverage. In this paper, a cell-search scheme is proposed for time-critical industrial IoT over mobile networks operating in high frequency bands. To achieve high timing accuracy under the increased hardware impairments, primary synchronization signals are designed based on the distributed concatenations of a Zadoff-Chu sequence and its modification. Next, a secondary synchronization signal is designed based on the distributed concatenation of a Kasami sequence and its modification, which provides larger set of cell IDs and is robust to the impairments. Compared to 5G NR under the increased hardware impairments, our analysis and evaluation show that the proposed cell-search scheme has advantages such as 25 % lower timing detection complexity, 150 % larger set of cell IDs, up to 15 dB and 6 dB signal-to-noise ratio gain in terms of timing and cell ID detection performance, respectively, and 60 % shorter cell-search time, thereby realizing 80 % lower battery consumption.

Index Terms—Carrier frequency offset, cell identification, OFDM system, phase noise, time synchronization.

I. INTRODUCTION

The global *Internet of Things* (IoT) market is expected to experience an explosive growth from US$ 381.30 billion in 2021 to US$ 1,854.76 billion in 2028 [1]. The fourth-generation (4G) Long-Term Evolution (LTE) already had the provision for IoT, but IoT has really become a major area of application of mobile communications in the incarnation of the fifth-generation (5G) cellular network, where *massive machine-type communication* (mMTC) and *ultra-reliable and low-latency communication* (URLLC) have been specified as two of the three 5G usage scenarios [2].

With the recent breakthrough in technologies such as machine learning, telecommunications, and semiconductor manufacturing, our "machines" are getting smarter, more efficient, and more connected every day. It is believed that the connectivity will play a key role in Industry 4.0 by providing significant operational cost savings [3]. On the other hand, people are spending more and more time in virtual worlds, and *Metaverse*, the future of Internet, will obscure the boundaries between virtual worlds and the real world.

These industrial and cultural trends assume that persistent connectivity with unprecedented precision, reliability, and scalability is available in the future network. For example, the time-sensitive networking (TSN) proposed by IEEE 802.1 working group achieved a nanosecond level of time synchronization to support time-critical machine-type communication (tcMTC) systems [4]. The same level of time synchronization as TSN would be required in future mobile networks [5]. As another example, localization or positioning accuracy in 5G systems has reached meter levels, and a standardization based on time difference of arrival is underway to improve accuracy up to the 20-centimeter level [6]. To support the use cases such as digital twins of manufacturing environments or cooperative industrial robots that require localization accuracy below 10 centimeters [7], [8], a sub-nanosecond level of time resolution may be required. Precise timing is also a critical ingredient of the virtual worlds of Metaverse.

What can be achieved with existing mobile systems such as 4G LTE [9]–[11] and 5G New Radio (NR) [12] may not be enough to meet the requirements of the applications and services of the future. In general, wider bandwidth and massive array beamforming are required to ensure more precise resolution. For instance, sixth-generation (6G) is expected to allocate bandwidth of a few gigahertz to meet the requirements of high resolution of the most stringent tcMTC applications of the future [8]. It may be impossible to secure such a wide frequency band in already crowded sub-6GHz frequency spectrum. Over-6GHz frequency spectrum, e.g., frequency range 2-2 (FR2-2) spectrum in range from 52.5 to 71 GHz expanded in Rel-17 [13] or sub-THz spectrum is preferred to sub-6GHz.

However, timing synchronization and cell identification in an over-6GHz wireless industrial IoT systems are required to be robust against the increased hardware (HW) impairments such as carrier frequency offset (CFO) and phase noise (PhN) caused by the higher carrier frequency [14]–[16]. When a carrier frequency is doubled, the value of CFO for a given

oscillator precision tolerance and the power spectral density of PhN increase by 3 dB and 6 dB [14], [17], respectively. Other impairments such as direct current (DC) offset and I-Q imbalance are not considered in this work because they are expected to be practically overcome by HW design techniques in which no reference signal is specified [12], [13].

More cell identification is required to mitigate the problem of physical cell identity (PCI) collision and confusion [5] by providing a sufficiently large number of PCIs. 5G NR has already been designed to support challenging usage scenarios such as indoor hot-spot and factory automation. These scenarios usually require dense deployment of a large number of small cells, and to support these scenarios, 5G NR has defined 1008 PCIs, twice the number of PCIs defined in 4G LTE. As discussed above, however, with a wider adoption of IoT supported by the future generation mobile networks, new IoT applications with even more stringent requirements are expected to show up. For example, it has been claimed that 6G should be able to facilitate up to 10 devices per cubic meter with link reliability of $(1 - 10^{-9})$ [5]. To guarantee much higher reliability and scalability than 5G NR [18], the cell coverage of mobile networks operating in high frequency bands is expected to be much smaller than that of 5G NR to combat shadowing effects. Moreover, it is crucial in bands above 6 GHz to use multiple antenna technologies such as massive antenna array beamforming. Sharp beamforming at both transmitter and receiver can greatly reduce the extra path loss in higher frequency bands [19]. Unfortunately, the distance that a sharp beam can reach in a direct path is much larger than the reduced cell coverage, which results in the increased number of cells that can interfere with one another. Thus, to reduce the inter-cell interference problems including PCI collision and confusion, 6G may need to have a larger set of PCIs.

Any device accessing the 5G NR system must find and be connected to a cell. The procedure consists of two steps. First, the device performs timing detection using the primary synchronization signal (PSS) received from a cell. Second, the device performs PCI detection using the secondary synchronization signal (SSS) from the cell with an aid of the already received PSS. Every cell has a unique {PSS, SSS} combination corresponding to a PCI index which is transmitted in the synchronization signal (SS) block. This two-step procedure is called *cell search* in 5G NR. In the first step of cell search, however, the device is unaware of the CFO between the cell and itself. The unknown CFO is a well-known source of inter-channel interference (ICI), but the PhN also becomes a significant source of ICI at a higher carrier frequency.

Various studies on cell search can be found in the literature [20]–[34]. While most of the studies focused on timing and PCI detection, there are few studies available on the robustness of cell search against PhN and PCI set expansion. The authors of [20]–[29] proposed efficient timing-detection techniques in the framework of the standards of LTE and NR. The studies recommended cross-correlation based timing-detection schemes over auto-correlation based timing-detection schemes for an improved timing accuracy. However, the cross-correlation based schemes tend to suffer performance degradation when there exists harsh CFO or PhN, in which case the auto-correlation based schemes can be preferred. The authors in [29] showed that even the auto-correlation based algorithm using cyclic prefix provided significant performance degradation for the higher CFO corresponding to the half of subcarrier spacing (SCS). Also, performing cross-correlation is computationally much more involved than performing auto-correlation. The authors of [30]–[33] conducted studies on the design of synchronization signals for cross-correlation based detection schemes. However, the synchronization signals designed in [30]–[32] addressed the problems of cross-correlation based timing detection schemes without any improvement in the detection complexity. The authors of [33] achieved both high timing accuracy and low detection complexity with a synchronization signal based on centrally symmetric localized concatenation. The performance of the synchronization signal proposed in [33] will be evaluated in this study to compare timing accuracy with the proposed scheme under the increased HW impairments. To address the high probability of false PCI detection in LTE SSS at a low signal-to-noise ratio (SNR), the authors in [34] proposed the SSS signal adopted in NR and an efficient detection method to obtain PCI using the SSS with the help of NR PSS. Specifically, they demonstrated the superiority of NR SSS over LTE SSS. That is, NR SSS doubled the total number of distinguishable PCIs compared to LTE SSS while improving PCI detection accuracy.

Contribution of this work: This paper proposes synchronization signals designed to be employed for cell search in mobile networks that operate at higher carrier frequencies.[1] For the convenience of explanation, the system employing the proposed SS block is called beyond radio (BR) to distinguish it from NR. Our contributions are summarized as follows:

- For timing detection, we propose two PSS signals. The proposed signals are constructed by the distributed concatenation of a Zadoff-Chu sequence and its modified sequence in frequency domain. As demonstrated in the analysis and evaluation, the proposed PSS signals are robust against CFO and PhN, while requiring low complexity in PSS detector implementation. We provide a mathematical analysis of the detection complexity in time domain. Also proposed is a 2-stage selection procedure for the best three PSS sequence indices in terms of robustness against CFO and PhN.

- For PCI detection, we propose an SSS signal that is built by the distributed concatenation of a Kasami sequence and its modified sequence in frequency domain. The proposed SSS signal has a larger set of distinguishable PCIs, and lower PCI detection complexity than NR SSS. BR SSS also provides the robustness against the increased HW impairments by exploiting the dominant ICI terms caused by the impairments as a diversity gain.

- A single dwell cell-search process and the corresponding state diagram based on the double detection thresholds

---

[1] The proposed synchronization signals can be used with the timing and PCI detection schemes proposed in [20]–[29], [34], to further improve the performance of cell search.
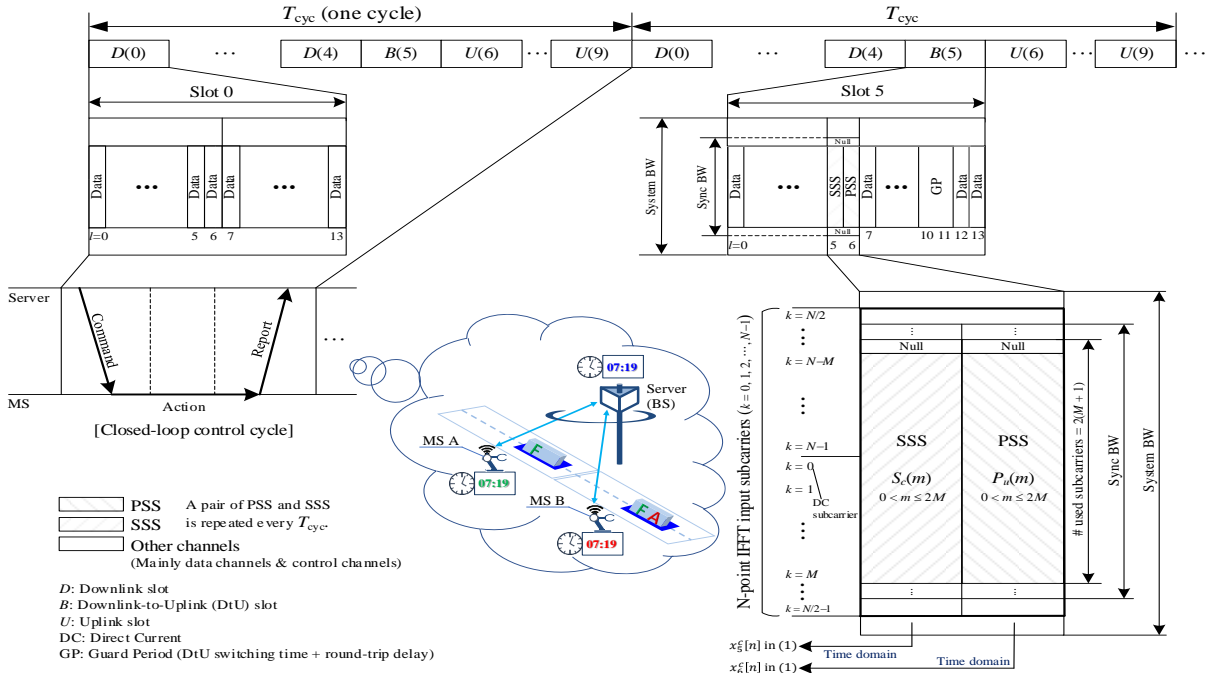
Fig. 1. TDD-based physical-layer cycle structure considered in this study.

of PSS and SSS detectors are proposed to evaluate the average and standard deviation of cell-search time and to compare the battery consumption between the synchronization schemes. From the evaluation, it is shown that the shortest cell-search time and lowest battery consumption are simultaneously achieved by only setting the SSS detection threshold without any PSS detection thresholds.

The remainder of this paper is organized as follows. Section II describes the system considered in this work. In Section III, the PSS and SSS signals of NR and BR are specified, a selection procedure of BR PSS sequence indices is proposed, and analyses regarding PSS and SSS are performed. Section IV describes PSS and SSS detectors, and analyzes detector complexity, cell-search time, and computing power. In Section V, through evaluation, we compare BR with other existing schemes in terms of detection error rate, root mean square of sample time offset, cell-search time, and computing power, followed by conclusions drawn in Section VI.

Notation: x and $\mathbf{x}$ denote the scalar and the vector (or the matrix), respectively. x^H, $\mathbf{x}^H$, and $\mathbf{x}^T$ denote the conjugate of x, the conjugate transpose of $\mathbf{x}$, and the transpose of $\mathbf{x}$, respectively. The operator diag$\{\cdot\}$ denotes the diagonal matrix. The operator $\lfloor x \rfloor$ denotes the floor function of real scalar x. The operator $[x]_n$ is the remainder after dividing integer x by integer n, which can be also expressed as the modulo operation $x \bmod n$.

II. SYSTEM DESCRIPTION

A factory automation system operating on the wireless network involves real-time interactions between multiple mobile stations (MSs) (e.g., robots, actuators, sensors) [35], [36]. It requires a specification reliable for stringent timing and PCI accuracies under HW impairments and an operating procedure to realize a periodic closed-loop control cycle mechanism of command-action-report.

To support the requirements, a time division duplex (TDD) based physical-layer frame structure, where the *frame* can be called the *cycle* in factory automation since it is repeated periodically, is presented in this study as illustrated in Fig. 1. This frame structure is able to chronologically follow the closed-loop control cycle with determinability and isochronosity. On top of this structure, an example of specification and operating procedure therein is provided as follows. In the specification, a cycle consists of 10 slots, and every slot occupies 14 orthogonal frequency division multiplexing (OFDM) symbols $l = 0, 1, 2, ..., 13$. To reflect the closed-loop control cycle mechanism, the cycle time repeated periodically is composed of Command period, Action period, and Report period. Command period consists of 4 downlink slots $D(0), ..., D(3)$. The symbols in the slots contain command data. Action period consists of 1 downlink slot $D(4)$, 1 downlink-to-uplink slot $B(5)$, and 1 uplink slot $U(6)$. $B(5)$ consists of 10 downlink OFDM symbols, 1 guard period (GP) occupying 2 OFDM symbols, and 2 uplink OFDM symbols. $D(4)$ and the downlink symbols in $B(5)$ carry the system control information related to initial system-access/system-maintenance and the synchronization signals related to timing/PCI detection. During the GP, downlink is switched to uplink. After the GP, $U(6)$ and the uplink symbols in $B(5)$ carry the system control information related to random access/acknowledgement and the physical-layer signals related to random-access and channel sounding. Report period consists of 3 uplink slots $U(7)$, $U(8)$, and $U(9)$. The symbols in the slots contain response data to action. In parallel, to maximize resource efficiency, a sequential or isochronous action during Action period (or a whole of periods within a cycle) according to the command acquired from Command period is performed.

In an initial operational procedure, using the synchronization signals of PSS and SSS in $B(5)$ as shown in Fig. 1, MS synchronizes under a high CFO and a high PhN, and

acquires a serving PCI under a low remaining CFO and a high PhN, and then obtains the information for an initial system access in $D(4)$. After that, a random-access procedure is performed using $B(5)$ and $U(6)$ to complete the initial system connection. In a non-initial operational procedure, the MS reliably maintains precise timing and continuously performs the closed-loop control cycle mechanism mentioned above under a low remaining CFO and a high PhN.

The cell search is performed during the initial access. In slot $B(5)$, as shown in Fig. 1, the SS block carries the synchronization signals SSS and PSS located in the 6-th and 7-th (i.e., $l = 5$ and 6) symbols, respectively. For example, NR synchronization signals in the SS block occupy 127 subcarriers including DC and 17 null subcarriers on either side. For a fair comparison of timing/PCI detection complexity and robustness against HW impairments between NR and BR synchronization signals, these signals are assumed to occupy the identical subcarriers in this work. On the assumption that in the initial system-access setup state an MS filters only the subcarriers that the SS block occupies while other subcarriers are ideally nulled, the inverse fast Fourier transform (IFFT) size N of the MS is 256 which is the minimum size, and the cyclic prefix (CP) duration N_{cp}^l to be 20 for symbols $l = 0, 7$ and 18 for symbols $l = 1, 2, ..., 6, 8, 9, ..., 13$.

Let $X_l^c(k)$ be the baseband transmit (Tx) frequency-domain (FD) signal at subcarrier k, where $c \in \{0, 1, \cdots, \Xi - 1\}$ represents a PCI index for the number of PCIs Ξ. For example, $\Xi = Q \times G$ in NR [12], where the number of physical identities (PIDs) Q and cell group identities (CGIs) G are 3 and 336, respectively. The corresponding baseband Tx time-domain (TD) signal $x_l^c(n)$ at sample n is expressed as

$$x_l^c(n) = \sqrt{\frac{N}{\mho}} \sum_{k=0}^{N-1} X_l^c(k) e^{j \frac{2\pi k(n - N_{cp}^l)}{N}}, \ 0 \le n < (N_{cp}^l + N), \quad (1)$$

where the subcarrier index k is illustrated in Fig. 1, and $\mho$ is the number of used subcarriers on which the data is actually loaded. $\mho = 2M + 1$ for 5G NR PSS/SSS as well as the random data, and $\mho = 2M$ for BR PSS1/PSS2/SSS, where M is the length of a base sequence for each of BR PSS1 and BR PSS2. $S_c(m)(0 \le m \le 2M)$ and $P_u(m)(0 \le m \le 2M)$ for the used subcarrier index m in Fig. 1 are the SSS and PSS FD signals corresponding to $X_5^c(k)$ and $X_6^c(k)$ in OFDM symbols 5 and 6 in slot 5, respectively, where the subscript $u \in \{0, 1, ..., Q - 1\}$ represents a PID index. Note that $X_l^c(k)$ for all used subcarriers in the slots except for slot 5 is assumed to be random data, and the average power of $x_l^c(n)$ is normalized to 1 due to the factor $\sqrt{N/\mho}$ in (1). The $(N_{cp}^l + N) \times 1$ vector form of (1) is expressed as

$$\mathbf{x}_l^c = \mathbf{F}^{-1} \begin{bmatrix} \mathbf{X}_{l,+}^c & \mathbf{0}_f & \mathbf{X}_{l,-}^c \end{bmatrix}^T = \begin{bmatrix} \mathbf{x}_{cp,l}^c & \mathbf{x}_{e,l}^c \end{bmatrix}^T, \quad (2)$$

$$\mathbf{X}_{l,+}^c = \begin{bmatrix} X_l^c(0) & X_l^c(1) \cdots X_l^c(M) \end{bmatrix},$$
$$\mathbf{X}_{l,-}^c = \begin{bmatrix} X_l^c(N-M) & X_l^c(N-M+1) \cdots X_l^c(N-1) \end{bmatrix},$$
$$\mathbf{x}_{cp,l}^c = \begin{bmatrix} x_l^c(0) & x_l^c(1) & \cdots x_l^c(N_{cp}^l - 1) \end{bmatrix},$$
$$\mathbf{x}_{e,l}^c = \begin{bmatrix} x_l^c(N_{cp}^l) & x_l^c(N_{cp}^l + 1) \cdots x_l^c(N_{cp}^l + N - 1) \end{bmatrix},$$
$$\left(\mathbf{F}^{-1} \right)_{n,m} = \sqrt{\frac{N}{2M+1}} e^{j \frac{2\pi(n - N_{cp}^l)m}{N}},$$

where $\mathbf{0}_f$ is the $1 \times f$ zero vector with $f = N - 2M - 1$, $\mathbf{F}^{-1}$ is the $(N_{cp}^l + N) \times N$ IFFT matrix, and $\mathbf{x}_{cp,l}^c$ and $\mathbf{x}_{e,l}^c$ are the $1 \times N_{cp}^l$ and $1 \times N$ baseband Tx TD signal vectors corresponding to CP and effective OFDM symbol, respectively.

Considering a time-varying frequency-selective fading channel, the $(N_{cp}^l + N) \times 1$ baseband receive (Rx) signal vector $\mathbf{r}_l^a$ corresponding to $\mathbf{x}_l^c$ in (2) with Rx antenna index a is

$$\mathbf{r}_l^a = \sqrt{P_s^c} \mathbf{E}_l^{a,c} \mathbf{H}_l^{a,c} \mathbf{x}_l^c + \sum_{c' \ne c} \sqrt{P_s^{c'}} \left\{ \mathbf{E}_l^{a,c'} \mathbf{H}_l^{a,c'} \mathbf{x}_l^{c'} \right\}$$
$$+ \begin{bmatrix} \mathbf{z}_{cp,l}^a & \mathbf{z}_{e,l}^a \end{bmatrix}^T = \begin{bmatrix} \mathbf{r}_{cp,l}^a & \mathbf{r}_{e,l}^a \end{bmatrix}^T, \quad (3)$$

where $\mathbf{r}_{cp,l}^a$ and $\mathbf{r}_{e,l}^a$ are the $1 \times N_{cp}^l$ and $1 \times N$ baseband Rx TD signal vectors corresponding to CP and effective OFDM symbol, respectively, and P_s^c is the average Rx power of the signal from cell c. Also, $\mathbf{z}_{cp,l}^a$ and $\mathbf{z}_{e,l}^a$ are the $1 \times N_{cp}^l$ and $1 \times N$ noise vectors whose elements are independent and identically distributed (i.i.d.) circular symmetric Gaussian random variables with noise variance N_0 corresponding to CP and effective OFDM symbol, respectively. $\mathbf{E}_l^{a,c}$ is the $(N_{cp}^l + N) \times (N_{cp}^l + N)$ diagonal matrix representing the CFO and PhN, and is given by $\text{diag} \{ E_l^{a,c}(0) \cdots E_l^{a,c}(n) \cdots E_l^{a,c}(N_{cp}^l + N - 1) \}$, where $E_l^{a,c}(n)$ is expressed as

$$E_l^{a,c}(n) = e^{j\left(\frac{2\pi \epsilon_c n}{N} + \varphi_c^l(n) \right)}, \quad (4)$$

where ϵ_c (abbreviated to ϵ for convenience in the sequel) is the CFO between cell c and MS normalized by SCS η. It can be seen that since ϵ is fixed, $\epsilon \cdot (n - 1)$ and $\epsilon \cdot n$ are highly correlated. The term $\varphi_c^l(n)$ representing PhN which is modelled Wiener process as an infinite impulse response filter is expressed as

$$\varphi_c^l(n) = \varphi_c^{l-1}(N_{cp}^{l-1} + N - 1) + \sum_{n'=0}^{n} \nu(n'), \quad (5)$$

where $\nu(n')$ is an i.i.d. Gaussian random variable with zero mean and variance $\sigma_\nu^2 = 2\pi\beta/N$ [17], [37], [38] for the PhN linewidth β normalized by SCS η. Furthermore, $\mathbf{H}_l^{a,c}$ in (3) is the $(N_{cp}^l + N) \times (N_{cp}^l + N)$ impulse response matrix of time-varying channel given by $(\mathbf{H}_l^{a,c})_{n,n'} = h_l^{a,c}(n, [n - n']_{N_{cp}^l + N})$ [31], [33], where $h_l^{a,c}(n, \xi)$ is the time-varying path gain of the ξth tap in sample n. Assuming $N_0 = 1$, SNR γ is identical to P_s^c in (3). Lastly, the second term of the first line in (3) is introduced to represent interferences coming from neighbor cells c', so that signal-to-interference ratio (SIR) is defined as $P_s^c / \sum_{c' \ne c} \{ P_s^{c'} \}$.

III. SIGNAL DESCRIPTION AND ANALYSIS

This section, firstly, describes the PSS and SSS signals of NR [12] and BR in frequency domain. Since the detection performances and complexities depend on the various parameters, both BR and NR share $Q = 3$, $M = 63$ such that $2M + 1 = 127$, $N = 256$ for a fair comparison. In specific, as the number of PID hypotheses Q increases, the detection performances degrade and the detection complexities increase. On the other hand, as M increases which is proportional to the number of used subcarriers for synchronization signals, their

detection performances improve but the complexities increase. CGI $g = \lfloor c/Q \rfloor$ in cell c, and PID $u = [c]_Q$ identifying one of Q cells for each CGI g, so that PCI c can be written as $c = Qg + u$. Second, a 2-stage procedure selecting the best three root indices of BR PSS sequence suitable for PIDs is proposed. Third, to prove the excellence of the proposed synchronization signals, we perform several analyses such as time-domain PSS signal-type and robustness against CFO and PhN. Also, BR SSS is compared with NR SSS in terms of the maximum number of PCIs, and robustness of cross-correlation property against fractional CFO and PhN.

Fig. 2. Frequency-domain structures of NR PSS/SSS and BR SSS.

A. NR Synchronization Signals

The PSS FD signal $\mathbf{P}_u$ of NR [12] as shown in Fig. 2(a) is given by

$$
\begin{aligned}
P_u(m) &= b_u(m) \qquad\qquad\qquad\qquad\qquad (6) \\
&= 1 - 2x_0\left([m + \mu_u]_{127}\right), \qquad 0 \le m \le 2M, \\
x_0(i+7) &= [x_0(i+4) + x_0(i)]_2, \\
[1110110] &= [x_0(6)\,x_0(5)\cdots x_0(1)\,x_0(0)].
\end{aligned}
$$

The NR PSS signal is based on binary phase shift keying (BPSK)-modulated length-127 maximal-length sequence (m-sequence). μ_u is the cyclic shift index of the m-sequence $\mathbf{x}_0$ corresponding to PID u with $\mu_0 = 0$, $\mu_1 = 43$, and $\mu_2 = 86$.

The SSS FD signal $\mathbf{S}_c$ as shown in Fig. 2(b) is constructed by an element-wise multiplication of two different BPSK-modulated length-127 cyclic-shifted m-sequences $\mathbf{x}_0$ and $\mathbf{x}_1$ as follows

$$
\begin{aligned}
S_c(m) &= [1 - 2x_0\left([m + m_0]_{127}\right)]\,[1 - 2x_1\left([m + m_1]_{127}\right)], \\
g_0 &= \lfloor g/112 \rfloor, \quad g_1 = [g]_{112}, \\
m_0 &= K(3g_0 + u), \quad m_1 = g_1, \\
x_0(i+7) &= [x_0(i+4) + x_0(i)]_2, \\
x_1(i+7) &= [x_1(i+7) + x_1(i)]_2, \qquad\qquad\qquad (7) \\
[0000001] &= [x_0(6)\,x_0(5)\cdots x_0(1)\,x_0(0)], \\
[0000001] &= [x_1(6)\,x_1(5)\cdots x_1(1)\,x_1(0)],
\end{aligned}
$$

where K is the minimum gap between any two distinct m_0, and the number of PCIs $\Xi = 336 \cdot \iota$ ($1 \le \iota \le \lfloor 127/(3K) \rfloor$). A set of the SSS FD signals each corresponding to PCI c is a union of a set of *cyclically distinct* sequences and sets of its cyclically shifted versions. Specifically, a set of cyclically

distinct sequences is generated by modulo-2 sum of $\mathbf{x}_0$ with a cyclic shift value m_0 and $\mathbf{x}_1$ with all possible cyclic shift values of m_1. For any $m_0' > m_0$, a set of cyclically shifted version of the above set by $(m_0' - m_0)$ is generated in the same way. This indicates that the number of PCIs Ξ can be defined as the product of the cardinality of a cyclically distinct sequence set and the number of distinct m_0. In NR [12], K in (7) is specified as 5 to mitigate false PCI detection, which is analyzed in Subsection III-E in detail. Given $K = 5$, $\Xi = 1008$ ($\iota = 3$) where the maximum value of Ξ is 2688 ($\iota = 8$).

Fig. 3. Frequency-domain structures of BR PSS1 and PSS2.

B. Proposed BR Synchronization Signals

In this section, firstly, based on a distributed concatenation of a Zadoff-Chu (ZC) base sequence[2] and its modified sequence, two PSS FD signals are proposed to reduce timing detection complexity and to increase robustness against CFO and PhN. Second, based on a distributed concatenation of a Kasami sequence and its modified sequence, an SSS FD signal is proposed to increase the number of PCIs and to be robust against ICI caused by CFO left after PSS detection and PhN.

The first proposed PSS (PSS1) FD signal $\mathbf{P}_u$ as shown in Fig. 3(a) is constructed by a distributed forward/reverse concatenation of length-M ZC sequence $\mathbf{b}_u$ and its reverse-order modified sequence $\tilde{\mathbf{b}}_u$ as

$$
P_u[m] = \begin{cases} b_u[\lfloor m/2 \rfloor], & 0 \le \text{even } m < 2M \\ \tilde{b}_u[M - 1 - \lfloor m/2 \rfloor], & 0 \le \text{odd } m < 2M, \end{cases} \qquad (8)
$$
$$
\text{with} \quad b_u[m] = e^{-j\frac{\pi \mu_u m(m+1)}{M}}, \quad 0 \le m < M,
$$

where $P_u(2M) = 0$, and μ_u is the root index of the length-M ZC base sequence $\mathbf{b}_u$ identifying PID u. $\tilde{\mathbf{b}}_u$ is specified as $-\mathbf{b}_u$ from a performance-oriented point of view.

The second PSS (PSS2) FD signal $\mathbf{P}_u$ as shown in Fig. 3(b) is constructed by a distributed half/half forward/reverse concatenation of length-M ZC sequence $\mathbf{b}_u$ and its forward/reverse-order negated sequence $\tilde{\mathbf{b}}_u$ as

$$
P_u(m) = \begin{cases} b_u(\lfloor m/2 \rfloor), & 0 \le \text{even } m < M \\ \tilde{b}_u(\lfloor m/2 \rfloor), & 0 \le \text{odd } m < M \\ b_u(M - 1 - \lfloor (m-M)/2 \rfloor), & M < \text{even } m \le 2M \\ \tilde{b}_u(M - 1 - \lfloor (m-M)/2 \rfloor), & M < \text{odd } m \le 2M, \end{cases} \qquad (9)
$$

[2] Note that if any binary or complex sequence serves the purpose of this study that is to realize a robustness against HW impairments and/or a low detection complexity, it can be adopted as a base sequence.

where $P_u(M) = 0$, and $\tilde{\mathbf{b}}_u$ is defined as in (8), and μ_u is also the root index of the length-M ZC base sequence identifying PID u. PSS2 achieves timing accuracy robust against HW impairments as much as PSS1, as well as computational detection complexity lower than PSS1. The determination of PID u and the detailed analysis of robustness against HW impairments for each of PSS1 and PSS2 will be held in Subsections III-C and III-D, respectively.

The SSS FD signal $\mathbf{S}_c$ with $\Xi = 1008 \cdot \iota \ (1 \leq \iota \leq \lfloor 63/(3K) \rfloor)$ as shown in Fig. 2(c) is constructed by a distributed for-ward/forward concatenation of BPSK-modulated signal $\mathbf{b}_c$ which is modulo-2 sum of three different cyclic-shifted length-63 m-sequences $\mathbf{x}_0$, $\mathbf{x}_1$, and length-7 m-sequence $\mathbf{x}_2$ and its modified signal $\tilde{\mathbf{b}}_c$ as follows

$$
\begin{aligned}
&\theta_c(m) = [x_0([m+m_0]_{63}) + x_1([m+m_1]_{63}) + x_2([m+m_2]_7)]_2, \\
&b_c(m) = 1 - 2\theta_c(m) \ \& \ \tilde{b}_c(m) = -b_c(m), \quad 0 \leq m < M, \\
&S_c(m) = \begin{cases} b_c(\lfloor m/2 \rfloor), & 0 \leq \text{even } m < M \\ \tilde{b}_c(\lfloor m/2 \rfloor), & 0 \leq \text{odd } m < M \\ b_c(\lfloor (m-1)/2 \rfloor), & M < \text{odd } m \leq 2M \\ \tilde{b}_c(\lfloor (m-1)/2 \rfloor), & M < \text{even } m \leq 2M, \end{cases} \quad (10) \\
&g_0 = \lfloor g/336 \rfloor, \quad g_1 = [g]_{48}, \quad g_2 = \lfloor [g]_{336}/48 \rfloor, \\
&m_0 = K(3g_0 + u), \quad m_1 = g_1, \quad m_2 = g_2,
\end{aligned}
$$

$$
\begin{aligned}
x_0(i+6) &= [x_0(i+1) + x_0(i)]_2, \\
x_1(i+6) &= [x_1(i+5) + x_1(i+2) + x_1(i+1) + x_1(i)]_2, \\
x_2(i+3) &= [x_2(i+2) + x_2(i)]_2, \\
[000001] &= [x_0(5)x_0(4) \cdots x_0(1)x_0(0)], \\
[101001] &= [x_1(5)x_1(4) \cdots x_1(1)x_1(0)], \\
[001] &= [x_2(2)x_2(1)x_2(0)],
\end{aligned}
$$

where $S_c(M) = 0$. A set of the SSS FD signals each corresponding to cell c can be generated in a similar manner as that in NR SSS. A set of cyclically distinct sequences is generated by modulo-2 sum of $\mathbf{x}_0$ with a given cyclic shift value m_0 and cyclically shifted versions of $\mathbf{x}_1$ and $\mathbf{x}_2$. For any $m_0' > m_0$, a set of cyclically shifted version of the above set by $(m_0' - m_0)$ is generated in the same way. If coefficient K is given as 5 as NR SSS in (7), the maximum value of Ξ is 4032 ($\iota = 4$). BR SSS achieves the maximum Ξ larger than NR SSS, as well as the robustness against HW impairments. The detailed analyses of Ξ and robustness against HW impairments for BR SSS will be held in Subsection III-E.

C. Proposed PSS Sequence Selection

Let us answer the question "How should we select the best three root indices in the proposed BR PSS sequences?". The answer lies in HW impairments. On one hand, both CFO and PhN are common in terms of phase distortions of the received signal in time domain, with the only difference being whether the phase rotation is fixed or random within an OFDM symbol. These phase distortions will cause timing errors. However, inter-symbol interference (ISI) does not occur, as long as the timing error is within the half of absolute CP [39].

On the other hand, as peak-to-average power ratio (PAPR) becomes higher (i.e., as dynamic range becomes wider), an amplifier with wider linear range should be employed to avoid signal distortion. In general, however, synchronization signals provide lower PAPR values over Tx data signal due to the randomness of the data itself. Since transmitter uses an amplifier that covers the PAPR of the data, the PAPR is not counted as a criterion for synchronization signal design. Hence, a 2-stage procedure is proposed to effectively pick up the best three sequence indices from each BR PSS signal by observing the *effective auto-correlation* and the *effective cross-correlation* under the harsh HW impairments. In the procedure, only hardware impairments are considered, and a specific channel model or certain SNR level is not assumed for generalization.
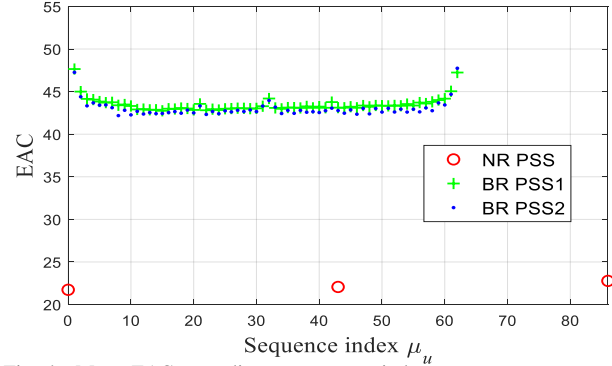

Fig. 4. Mean EAC according to sequence index.

Stage 1: To analyze robustness against HW impairments, the *effective auto-correlation* (EAC) $\Omega(\mu_u)$ within the last one-sixteenth of the CP duration, the sample points very close to perfect synchronization, is defined as

$$
\Omega(\mu_u) = \frac{1}{N\left(\left\lfloor \frac{N_{cP}^6}{16} \right\rfloor + 1\right)} \sum_{\varphi = \left\lfloor \frac{15 N_{cP}^6}{16} \right\rfloor}^{N_{cP}^6} \left| (\mathbf{x}_{\mu_u})^H \cdot \mathbf{r}_{\mu_u}[\varphi:(\varphi+(N-1))] \right|^2, \quad (11)
$$

$$
\mathbf{r}_{\mu_u} = \mathbf{E}_6^{0,c} \mathbf{x}_6^c(\mu_u),
$$

where $\mathbf{r}_{\mu_u}$ is the version of $\mathbf{r}_6^0$ at slot 5 and symbol 6 that considers CFO ϵ and PhN linewidth β modelled in (4) and (5) (i.e., $\mathbf{E}_6^{0,c}$) with single Rx antenna (i.e., $a = 0$) and excludes the interference (2nd term), the noise (3rd term), and the fading (i.e., $\mathbf{H}_6^{0,c} = \mathbf{I}_{N_{cP}^6 + N}$) in (3). $\mathbf{x}_6^c(\mu_u)$ and $\mathbf{x}_{\mu_u}$ are the $(N_{cP}^6 + N) \times 1$ and $N \times 1$ signal vectors representing the time-domain CP-added and CP-excluded PSS signals with the ZC sequence index μ_u coming from each of the frequency-domain PSS signals as shown in (8) and (9), respectively. $\mathbf{r}_{\mu_u}[\varphi:(\varphi+(N-1))]$ represents an $N \times 1$ sub-vector of $\mathbf{r}_{\mu_u}$ obtained by extracting N elements from $\mathbf{r}_{\mu_u}$ starting from φ. For analysis in the same line with the evaluation in Section VI, very large HW impairments of $\epsilon = 0.67$ [30], [33] and $\beta = 0.4$ are employed. Taking into consideration that frequency spectrum higher than FR2-2 band is expected to be allocated for more stringent tcMTC applications, and that PhN increases by 6 dB when a carrier frequency is doubled [14], [17], $\beta = 0.4$ is employed as the worst case, which is about 6 dB higher than $\beta = 1/12$ used in [38].

The mean EAC performance (i.e., $E\{\Omega(\mu_u)\}$) as a function of sequence index μ_u is shown in Fig. 4, where $E\{\cdot\}$ is the ensemble average operator. It is shown that both BR PSS1 and

PSS2 provide almost the same EAC performances and very higher EAC performances than NR PSS. From the results, the selected candidate sequence indices for both BR PSS1 and PSS2 are 1, 2, 61, and 62, since these indices provide at least 195 % higher EAC performances over NR PSS. The candidate index sets corresponding to the selected indices are {1,2,61}, {1,2,62}, {1,61,62}, and {2,61,62} each of which comprises 3 indices μ_0, μ_1, and μ_2. Considering the highest EACs are in indices 1 and 62, the consequent candidate index sets are reduced to {1,2,62} and {1,61,62}.

Stage 2: The *effective cross-correlation* (ECC) $\Lambda(\mu_u, \mu'_u)$ within the CP duration is defined as

$$\Lambda(\mu_u, \mu'_u) = \frac{1}{N\left(N_{CP}^6 + 1\right)} \sum_{\varphi=0}^{N_{CP}^6} \frac{\left|\left(\mathbf{x}_{\mu'_u}\right)^H \cdot \mathbf{r}_{\mu_u}[\varphi:(\varphi+(N-1))]\right|^2}{E\{\Omega(\mu_0, \mu_1, \mu_2)\}}, \quad (12)$$

where $\mu_u \neq \mu'_u$, and $E\{\Omega(\mu_0, \mu_1, \mu_2)\} = \frac{1}{3}\sum_{i=0}^{2} E\{\Omega(\mu_i)\}$ for given candidate index set $\{\mu_0, \mu_1, \mu_2\}$. Table I shows the mean ECC in which interference, noise, and fading are excluded as in Stage 1. It is shown that both BR PSS1 and PSS2 provide almost the same ECC values and about 50 % lower ECC values than NR PSS. A 2-stage selection procedure is as follows. First, candidate indices sets with lower $E\{\Lambda\}$'s are selected such that the gaps among the $E\{\Lambda\}$'s are lower to provide the similar level of inter-cell interference. Second, the indices set with the highest value of $E\{\Omega\}$ is selected if $E\{\Lambda\}$'s are almost the same. From the criterion, the best index set {1,61,62} for each of BR PSS1 and BR PSS2 is consequently selected.

TABLE I
MEAN ECC RESULTS.

(μ_u, μ'_u)	$E\{\Lambda\}$	(μ_u, μ'_u)	$E\{\Lambda\}$	(μ_u, μ'_u)	$E\{\Lambda\}$
NR PSS : {0,43,86}					
(0,43)	0.0629	(0,86)	0.0685	(43,86)	0.0611
BR PSS1 : {1,2,62}					
(1,2)	0.0444	(1,62)	0.0367	(2,62)	0.0376
BR PSS1 : {1,61,62}					
(1,61)	0.0379	(1,62)	0.0367	(61,62)	0.0447
BR PSS2 : {1,2,62}					
(1,2)	0.0423	(1,62)	0.0334	(2,62)	0.0360
BR PSS2 : {1,61,62}					
(1,61)	0.0349	(1,62)	0.0333	(61,62)	0.0437

D. Comparative Analysis regarding PSS Specification

*1) **Time-domain signal-type**:* A synchronization signal in time domain is used to perform timing detection since the frequency-domain signal cannot be obtained until a sample timing is detected. This implies that if a synchronization signal is either periodically null or real in time domain, its detection complexity is reduced. This fact lets us compare the proposed BR PSS time-domain signals with existing PSS time-domain signals in terms of signal type that are summarized in Table II, where AR stands for *Alternative Radio* in [33]. The table shows that BR PSS2 provides lower computational complexity of timing detection, which will be revisited when we discuss detector complexity in Subsection IV-C1.

TABLE II
TIME-DOMAIN SIGNAL TYPES OF PSS SIGNALS.

Signal	Type	Signal	Type
NR PSS	Complex	BR PSS1	Complex
AR PSS	Real	BR PSS2	Complex, Zero

The time-domain signals of NR PSS and BR PSS1 are complex, which comes from the inverse discrete Fourier transform (IDFT) property [40]. The time-domain signal of AR PSS [33] is real owing to the centrally symmetric concatenation in frequency domain. On the other hand, the time-domain signal of BR PSS2 is zero for one in every $N/(M+1)$ sample-time indices regardless of the sign of $\tilde{\mathbf{b}}_u$. We have the following proposition.

Proposition 1: The TD signal $\mathbf{x}_l^c$ of BR PSS2 FD signal $\mathbf{P}_u$ in (9) satisfies the following property.

$$x_l^c(n) = 0 \text{ for } n = (2\alpha - 1)\frac{N}{2(M+1)}, \ \alpha = 1, 2, \cdots.$$

Proof: Based on the symmetry of ZC (see (30)), the periodicity of IDFT (see Fig. 18 and (32)), and the concatenation rule of PSS2 (see (33)), Proposition 1 is proved (see Appendix A). ∎

*2) **Robustness against HW impairments**:* A longer sequence has a better cross-correlation property (i.e., a higher peak or lower sidelobe) in general, but is also more susceptible to HW impairments since it suffers from more phase rotation in time domain caused by the impairments. Often, these two are metrics of performance conflicting with each other. As a solution, a careful combination of two short half-length sequences to produce a long sequence in time domain can result in a sequence that is robust against HW impairments without sacrificing the cross-correlation property.

As described in Section III-B, each of PSS1 and PSS2 (called *BR PSS* here) is built by interleaving a base sequence $\mathbf{b}_u$ with its modified sequence $\tilde{\mathbf{b}}_u$ in frequency domain. The result is BR PSS whose time-domain signal is a superposition of two components as illustrated in Fig. 5. According to the property of IDFT output for odd input elements with zero-padded even input elements [40], the time-domain sequence composed of a repetition of $\mathbf{x}_1$ (i.e., $[\mathbf{x}_1, -\mathbf{x}_1]$ within an OFDM symbol as shown in Fig. 5) comes from the base sequence $\mathbf{b}_u$. According to the property of IDFT output for even input elements with zero-padded odd input elements [40], the time-domain sequence composed of a repetition of $\mathbf{x}_2$ (i.e., $[\mathbf{x}_2, \mathbf{x}_2]$ within an OFDM symbol as shown in Fig. 5) comes from the modified sequence $\tilde{\mathbf{b}}_u$. The correlation coefficient between the BR PSS in Fig. 5 and its corresponding received signal can be approximated as

$$\rho_{\mathbf{P}_u\mathbf{r}}^{\mathrm{BR}}[\tau] \approx 0.5\rho_{\mathbf{x}_1\mathbf{r}_1}[\tau] + 0.5\rho_{\mathbf{x}_2\mathbf{r}_2}[\tau], \quad (13)$$

for sufficiently small τ (i.e., close to the peak), where τ stands for sample time offset (STO) and means the difference between perfect sample time and detected sample time. $\mathbf{r}_1$ and $\mathbf{r}_2$ represent the received signals in which HW impairments are
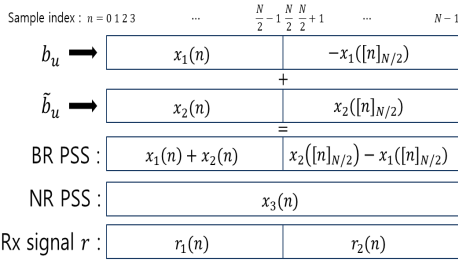
Fig. 5. Components of BR PSS and NR PSS in time domain.

embedded when $\mathbf{x}_1+\mathbf{x}_2$ and $\mathbf{x}_2-\mathbf{x}_1$ are transmitted, respectively. The correlation coefficient $\rho_{\mathbf{xr}}[\tau]$ between a reference signal $\mathbf{x}$ and a received signal $\mathbf{r}$ is defined as

$$\rho_{\mathbf{xr}}[\tau] = \frac{\sum_m x(m+\tau)r^H(m)}{\sum_m |x(m)| \sum_m |r(m)|}.$$

From the symmetry of ZC (see (30)), the frequency-reverse property of IDFT (see Fig. 18 and (32)), and the concatenation rule of BR PSS (see (33)), we have the following proposition.

Proposition 2: The first half TD signal $\mathbf{x}_1$ and $\mathbf{x}_2$ for each of BR PSS1 and PSS2 FD $\mathbf{P}_u$ in (8) and (9) have the following relation.

$$x_{2,\text{pss1}}(n) = \begin{cases} -x_{1,\text{pss1}}(n)e^{j\frac{2\pi n}{N}}, & 0 \le n < \frac{N}{2} \\ -x_{1,\text{pss1}}([n]_{N/2})e^{j\frac{2\pi[n]_{N/2}}{N}}, & \frac{N}{2} \le n < N, \end{cases} \quad (14)$$

$$x_{2,\text{pss2}}(n) \approx \begin{cases} -x_{1,\text{pss2}}(n)e^{j\frac{2\pi n}{N}}, & 0 \le n < \frac{N}{2} \\ -x_{1,\text{pss2}}([n]_{N/2})e^{j\frac{2\pi[n]_{N/2}}{N}}, & \frac{N}{2} \le n < N. \end{cases}$$

Proof: See Appendix B. ∎

By substituting (14) into (13), we obtain

$$\left|\rho_{\mathbf{P}_u\mathbf{r}}^{\text{BR}}[\tau]\right| = \left|0.5\rho_{\mathbf{x}_1\mathbf{r}_1}[\tau]\left(1 - e^{j\frac{2\pi\tau}{N}}\right)\right| \le \left|\rho_{\mathbf{x}_1\mathbf{r}_1}[\tau]\right|, \quad (15)$$

where the equality holds at the peak when $\tau = 0$. The inequality denotes that BR PSS has more suppressed sidelobes ($\tau\neq0$) compared to the shorter sequence $\mathbf{x}_1$, which makes BR PSS a *full-length* synchronization signal rather than a simple repetition of short signals. As mentioned earlier, a shorter sequence is less susceptible to HW impairments. Because $\mathbf{x}_1$ and $\mathbf{x}_2$ are shorter than 5G NR PSS (e.g., $\mathbf{x}_3$ in Fig. 5),

$$\rho_{\text{NRpss}}[\tau] < \rho_{x_1r_1}[\tau],\ \rho_{x_2r_2}[\tau] \le 1,$$

for $\tau = 0$ (at the peak). Thus, from (13),

$$\rho_{\mathbf{P}_u\mathbf{r}}^{\text{NR}}[0] < \rho_{\mathbf{P}_u\mathbf{r}}^{\text{BR}}[0] \le 1,$$

which shows the improved *detection* performance of BR PSS.

TABLE III
SUMMARY ON ROBUSTNESS AGAINST CFO/PHN.

	Average EAC	Average ECC
NR PSS	22.1933	0.0642
AR PSS	32.0937	0.0384
BR PSS1	46.6293	0.0376
BR PSS2	46.5613	0.0373

As a verification of the aforementioned theoretical analysis, Table III shows the average EAC and ECC performances

obtained from the results of Fig. 4 and Table I regarding NR PSS, AR PSS, BR PSS1, and BR PSS2. The EAC and ECC values are averaged over three mean EACs and ECCs for the selected best three indices, respectively. BR PSS1 and PSS2 provides higher average EAC and lower average ECC, outperforming AR and NR PSS in terms of the robustness to the impairments. The observation will be verified in Section V.

E. Analysis regarding SSS Specification

Assuming that an FD SSS signal $\mathbf{S}_c$ corresponding to PCI c in (7) for NR SSS or in (10) for BR SSS is transmitted, the FD received signal $\mathbf{R}_c$ of $\mathbf{r}_5^a$ at slot 5 and symbol 5 excluding the second term corresponding to inter-cell interference in (3) is given as

$$R_c(k) = \sum_m \sum_v \left\{ C_{[k-m]_N} P_{[m-v]_N} H(v) S_c(v) \right\} + Z(k), \quad (16)$$

$$C_i = \frac{1 - e^{j2\pi\epsilon}}{1 - e^{-j\frac{2\pi(i-\epsilon)}{N}}},$$

$$P_i = \frac{1}{N} \sum_n e^{j\varphi_c^5(n)} e^{-j\frac{2\pi ni}{N}},$$

where C_i and P_i are the FD coefficients of fractional CFO components such that $\epsilon \neq 0$ ($-0.5 \le \epsilon \le 0.5$) and PhN components φ_c^5 in (5), respectively, and $H(v)$ and $Z(k)$ are the FD channel coefficient and additive noise, respectively. Assume that $(2k_\epsilon+1)$ FD CFO components in $C \triangleq \{k - k_\epsilon, k - k_\epsilon + 1, \cdots, k + k_\epsilon\}$ and $(2k_\varphi+1)$ FD PhN components in $\mathcal{P} \triangleq \{k - k_\varphi, k - k_\varphi + 1, \cdots, k + k_\varphi\}$ dominantly affect subcarrier k as ICI. FD received signal $\mathbf{R}_c$ in (16) can be reformulated as

$$\begin{aligned} R_c(k) = &\ C_0 P_0 H(k) S_c(k) \\ &+ \sum_{(m,v)\in C\times\mathcal{P}\setminus(k,k)} C_{[k-m]_N} P_{[m-v]_N} H(v) S_c(v) \\ &+ \sum_{(m,v)\notin C\times\mathcal{P}} C_{[k-m]_N} P_{[m-v]_N} H(v) S_c(v) \\ &+ Z(k), \end{aligned} \quad (17)$$

where the first term represents the transmitted signal of subcarrier k affected by common phase error and CFO, the second term represents dominant ICI terms, and the third term corresponds to a negligible ICI term. SSS detection performance mainly depends on the cross-correlation distribution. Cross-correlation $\mathcal{S}(c')$ of FD received signal $\mathbf{R}_c$ and FD SSS signal $\mathbf{S}_{c'}$ corresponding to PCI hypothesis $c' \in \{0, \ldots, \Xi - 1\}$ can be calculated as

$$\mathcal{S}(c') = \left|\sum_{k=0}^{2M} S_{c'}(k)^H R_c(k)\right|^2. \quad (18)$$

For example, let $k_\epsilon = 1$, $k_\varphi = 0$, $H(k) = 1$, and $Z(k) = 0$. Three dominant FD CFO components in $C = \{k - 1, k, k + 1\}$ affect the sequence property and FD PhN coefficients $P_i = \delta(i)$. Then cross-correlation $\mathcal{S}(c')$ can be approximated as

$$\mathcal{S}(c') \approx \left| \begin{array}{l} C_0 \sum_{k=0}^{2M} S_{c'}(k)^H S_c(k) \\ +C_1 \sum_{k=0}^{2M} S_{c'}(k)^H S_c(k-1) \\ +C_{N-1} \sum_{k=0}^{2M} S_{c'}(k)^H S_c(k+1) \end{array} \right|^2. \quad (19)$$

Normalized cross-correlation (NCC) value represents the side-lobe value of cross-correlation $\mathcal{S}(c')$ such that $c' \neq c$ normalized to the peak cross-correlation output $\mathcal{S}(c)$. Fig. 6 represents maximum NCC value between two different sequences from an SSS sequence set according to various CFOs under the assumption of $k_\varphi = 0$, $H(k) = 1$, and $Z(k) = 0$. Maximum NCC value of NR SSS with $K = 1$ is about 0 dB at $\epsilon = 0.5$, which denotes that PCI $c' \neq c$ such that $S_{c'}(k) = S_c(k-1)$ has the same level of cross-correlation output $\mathcal{S}(c')$ as peak cross-correlation $\mathcal{S}(c)$. Peak cross-correlation output $\mathcal{S}(c)$ decreases with the value of C_0, while the sidelobe value increases with the value of C_1, as the fractional CFO increases. In addition, integer CFO $\epsilon = 1$ causes a cyclic shift in a frequency domain resulting in false PCI detection. Therefore, $K = 5$ is adopted in 5G NR SSS to be robust against various CFOs. NR SSS with $K = 5$ shows maximum NCC value of -2.6 dB at fractional CFO $\epsilon = 0.5$. The robustness against CFO comes at the expense of maximum Ξ, since Ξ are bounded by an inverse of K.
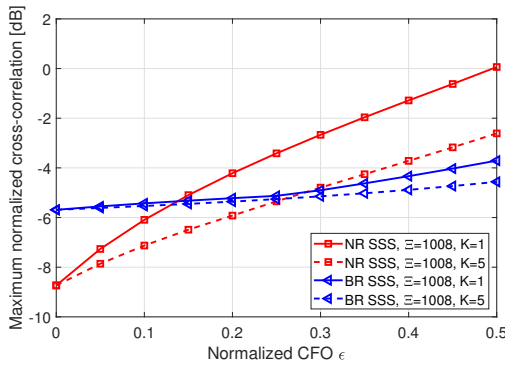

Fig. 6. Maximum normalized cross-correlation outputs of NR SSS and BR SSS according to various fractional CFOs.

On the other hand, the cross-correlation output of BR SSS can be reformulated into the cross-correlation of base sequence $\mathbf{b}_c$ in BR SSS as

$$\mathcal{S}(c') \approx \left| \begin{array}{l} (2C_0 - C_{N-1} - C_1) \sum_{m=0}^{M-1} b_{c'}(m)^H b_c(m) \\ -C_1 \sum_{m=0}^{M-1} b_{c'}(m)^H b_c(m-1) \\ -C_{N-1} \sum_{m=0}^{M-1} b_{c'}(m)^H b_c(m+1) \end{array} \right|^2 . \quad (20)$$

For the cross-correlation output of NR SSS in (19) where the peak term is affected only by C_0, the peak term decreases significantly as the fractional CFO increases. However, the peak term of base sequence $\mathbf{b}_c$ in (20) of BR SSS is scaled by coefficient $(2C_0 - C_{N-1} - C_1)$. The three dominant components in the coefficient are combined constructively in various fractional CFO environments, which makes the peak term more robust to fractional CFOs compared to NR SSS. In other words, the distributed concatenation of the base sequence and its modification allows the sequence to capture higher diversity order and robustness in a high fractional CFO regime. The diversity gain is achieved at the cost of 3 dB degradation of maximum NCC value at $\epsilon = 0$ than NR SSS due to the worse cross-correlation property of the short-length Kasami sequence. The sidelobe values of cross-correlation output $\mathcal{S}(c')$ such that $c' \neq c$ in (20) are the weighted sum of cross-correlation outputs following the cross-correlation

distribution, which is also robust to fractional CFO. Hence, BR SSS with $K = 1$ is robust to fractional CFO, providing the maximum NCC value of -3.7 dB at $\epsilon = 0.5$. $K = 5$ is adopted for BR SSS in this paper to guarantee the same level of robustness to integer CFOs as NR SSS. BR SSS with $K = 5$ provides maximum NCC value of -4.6 dB at $\epsilon = 0.5$ that is 2.0 dB lower than NR SSS with $K = 5$. Same diversity gain of BR SSS can be observed under high PhN that will be shown in Section V.

TABLE IV
COMPARISON FOR NUMBER OF PCIS Ξ BY DIFFERENT K.

	Maximum Ξ by $K = 1$	Maximum Ξ by $K = 5$
NR SSS	$126 \times 112 = 14112$	$24 \times 112 = 2688$
BR SSS	$63 \times 48 \times 7 = 21168$	$12 \times 48 \times 7 = 4032$

Table IV compares the maximum number of PCIs Ξ by the mapping between cyclic shift values and PCIs with $K = 1$ and $K = 5$. It is assumed that the number of distinct m_0 is a multiple of 3 since m_0 is a function of PID u, and the cardinality of a cyclically distinct sequence set is a multiple of 112 for comparison with NR SSS. BR SSS provides 1.5 times maximum Ξ larger than NR SSS with the same parameter.

IV. DETECTOR DESCRIPTION AND ANALYSIS

A. PSS Detector for the Proposed BR System

To maximize the performance of timing estimation [11], [21], [41], [42], the maximum likelihood (ML) estimate of STOs can be used, where the meaning of STO τ is the difference between perfect sample time and detected sample time once again. The ML estimate is implemented as a replica-correlation scheme in this work.
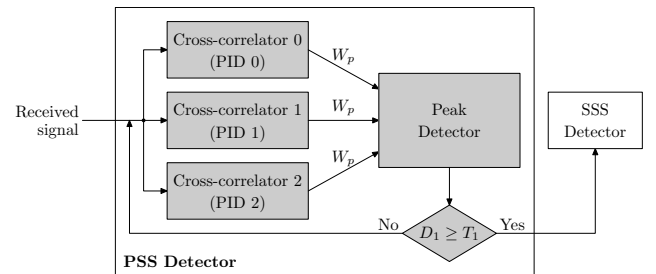

Fig. 7. Block diagram of PSS detector.

As shown in Fig. 7, the detector consists of three cross-correlators for PID $u = 0, 1, 2$, a peak detector, and a comparator. The complex-valued (real-valued) output $R_{\phi,u}$ ($\check{R}_{\phi,u}$) of cross-correlator u for sample time ϕ is defined as

$$R_{\phi,u} = \sum_{a=0}^{A-1} \left\{ \frac{\left(\mathbf{x}_{6,\mu_u}^c (N_{cp}^6) \right)^H \cdot \mathbf{r}_6^a [\phi : (\phi + (N-1))]}{N} \right\},$$

$$\check{R}_{\phi,u} = \left| R_{\phi,u} \right|^2, \quad (21)$$

where A is the number of Rx antennas. The sample time is in range of $0 \leq \phi < W_p$, where W_p represents the window size of PSS detector, and is the total number of samples in one cycle frame duration as shown in Fig. 1. $\check{R}_{\phi,u}$ flows into the

peak detector as an input. The pair of sample time instant $\hat{\phi}$ and PID $\hat{u}$ are detected such that

$$(\hat{\phi}, \hat{u}) \;=\; \arg \max_{\phi, u} \breve{R}_{\phi, u}. \tag{22}$$

If $(\hat{\phi}, \hat{u})$ is the actual start sample time ϕ and PID u of PSS TD signal excluding CP, the perfect time synchronization (i.e., detected STO $\hat{\tau} = \hat{\phi} - \phi = 0$ and $\hat{u} = u$) is realized. To determine whether the PSS detection is completed or not, a decision variable D_1 is defined as

$$D_1 \;=\; \frac{\breve{R}_{\hat{\phi}, \hat{u}}}{\sum_{(\phi, u) \neq (\hat{\phi}, \hat{u})} \frac{\breve{R}_{\phi, u}}{W_p \cdot Q - 1}}. \tag{23}$$

If $D_1 \geq T_1$ where T_1 is the predefined PSS detection threshold, the PSS detection is completed and the SSS detection starts. Otherwise, the PSS detection is performed again. Note that The numerator and denominator in (23) can be regarded as the average powers of a signal term and a noise term, respectively, so that D_1 can be viewed as SNR. The denominator of (23) makes D_1 independent of the automatic gain control (AGC) level [43]. Also Note that since the probability distribution function (PDF) of $\breve{R}_{\phi, u}$ is unknown due to the unknown PDF of the product of the fading channel and the time-domain signal, the PDF of $(\hat{\phi}, \hat{u})$ in (22) is unable to be obtained any more. Although the PDF of $\breve{R}_{\phi, u}$ is known, the PDF of $\breve{R}_{\hat{\phi}, \hat{u}}$ is still unknown because the PDF of the argument maxima function is unknown. Thus, the theoretical timing detection probability of PSS will be reserved for further research.

B. SSS Detector for the Proposed BR System

As shown in Fig. 8, the SSS detector consists of a CFO estimator/compensator, an N-point FFT & extractor, a cross-correlator, a peak detector, and a comparator.
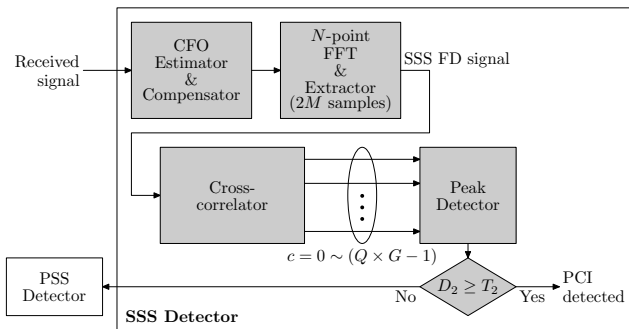

Fig. 8. Block diagram of SSS detector.

First, the SSS detector estimates CFO $\hat{\epsilon}$ in the CFO estimator [31], [43] using $\hat{\phi}$ and $R_{\hat{\phi}, \hat{u}}$. After that, $\hat{\epsilon}$ is compensated for the received signal. Second, N-point FFT is performed from the start sample time $\hat{\phi} - (N_{cp}^6 + N)$. Then, the received SSS FD signal $\mathbf{R}_c$ in (16) includes fading channel, noise, residual CFO, and PhN. Third, passing through the cross-correlator, $\mathcal{S}(c')$ in (18) is obtained for every PCI hypothesis c'. Fourth, as shown in Fig. 8, $\mathcal{S}(c')$ flows into the input of the peak detector. PCI $\hat{c}$ is detected such that

$$\hat{c} \;=\; \arg \max_{c'} \mathcal{S}(c'). \tag{24}$$

To determine whether the SSS detection is completed or not, a decision variable D_2 is defined as

$$D_2 \;=\; \frac{|\mathcal{S}(\hat{c})|^2}{\sum_{c' \neq \hat{c}} \frac{|\mathcal{S}(c')|^2}{\Xi - 1}}. \tag{25}$$

If D_2 is equal to or greater than the predefined SSS (detection) threshold T_2, cell search is completed. Otherwise, the PSS detection is performed again. As in the PSS detector, the denominator of (25) makes D_2 independent of the AGC level. Similarly, as noted in Subsection IV-A, since the PDFs of $\mathcal{S}(c')$ and its argument maxima function in (24) are unknown, the PDF of $\hat{c}$ is unable to be obtained any more. Thus, the theoretical PCI detection probability of SSS will be reserved for further research as well.

C. Detector Complexity

1) Computational complexity of PSS detector: The most computationally intensive part of cell search is in the PSS detector. For all of NR, AR, and BR, the ML timing estimation defined in (21) and (22) is employed in the PSS detector. Table V compares computational complexities in units of millions of operations per second (MOPS) to evaluate the computing power $\$_p$ of PSS detector [33], [44] as a function of SCS η, FFT size N, and M.[3] For the minimum FFT size $N = 256$, AR PSS provides 49.88 % lower computing power over NR PSS and BR PSS1. BR PSS2 provides 24.94 % lower computing power over NR PSS and BR PSS1. AR PSS provides 33.23 % lower computing power than BR PSS2. Consequently, AR PSS has the lowest computational complexity over other PSSs. However, BR PSS2 provides lower computing power required for cell search considering timing detection performance than AR PSS under the harsh HW impairments, as will be shown in Subsection V-C.

TABLE V
COMPUTATIONAL COMPLEXITIES OF PSS DETECTORS.

	$\$_p$ [MOPS]
NR PSS & BR PSS1	$\approx 10^{-6} \eta N (36N + 22)$
AR PSS	$\approx 10^{-6} \eta N (18N + 22)$
BR PSS2	$\approx 10^{-6} \eta N (36(N - M - 1) + 22)$

TABLE VI
COMPUTATIONAL COMPLEXITIES OF SSS DETECTORS.

	$\$_s$ [MOPS]
NR SSS	$\approx 10^{-6} (\eta/150)(2N \log_2 N + 19.125\Xi)$
BR SSS	$\approx 10^{-6} (\eta/150)(2N \log_2 N + 18.238\Xi)$

2) Computational complexity of SSS detector: Table VI compares NR SSS with BR SSS in terms of computational complexity in units of MOPS to evaluate the computing power $\$_s$ of SSS detector as a function of SCS η, FFT size N, and

---

[3]In this table, the complexities of three cross-correlators as shown in Fig. 7 are on the assumption that one real addition, one real multiplication, and one squared root need 1, 8, and 6 operations, respectively, from which the number of operations needed for each of complex addition and multiplication is calculated.

number of PCIs Ξ. Each of NR and BR SSS sequences is constructed by modulo-2 sum of cyclically shifted m-sequences whose cross-correlation can be implemented through permutation and fast Walsh-Hadamard transform (FWHT) [45]. Computational complexities of SSS detection including N-point FFT and FWHT-based cross-correlation are compared between NR SSS and BR SSS in Table VI. For cross-correlation of NR SSS, there are $(\Xi/112)$ possible cyclic shift values of m_0, and 112 possible cyclic shift values of m_1 for each m_0. Cross-correlation of the received signal and each of $(\Xi/112)$ cyclically shifted versions of $\mathbf{x}_0$ requires $(\Xi/112) \cdot (127 - 1)$ additions. Then, cross-correlation between each of the $(\Xi/112)$ remaining received signals and 127 cyclically shifted versions of $\mathbf{x}_1$ are calculated by FWHT, which requires $127 \cdot \log_2 128$ additions [34].

For cross-correlation regarding BR SSS, there exist $(\Xi/336)$ possible cyclic shift values of m_0, 48 possible cyclic shift values of m_1 for each m_0, and 7 possible cyclic shift values of m_2 for each m_0 and m_1. Cross-correlation of the received signal and each of $(\Xi/336)$ cyclically shifted versions of $\mathbf{x}_0$ requires $(\Xi/336) \cdot (63 - 1)$ additions per base sequence. Then, cross-correlation between each of the $(\Xi/336)$ remaining received signals and 63 cyclically shifted versions of $\mathbf{x}_1$ are calculated by FWHT requiring $63 \cdot \log_2 64$ additions. Lastly, cross-correlation between each of the $(\Xi/336) \cdot 48$ remaining received signals and 7 cyclically shifted versions of $\mathbf{x}_2$ are implemented by FWHT requiring $7 \cdot \log_2 8$ additions. For identical $\Xi = 1008$ and the minimum FFT size $N = 256$ as a baseline, BR SSS gives 3.83 % lower complexity than NR SSS.
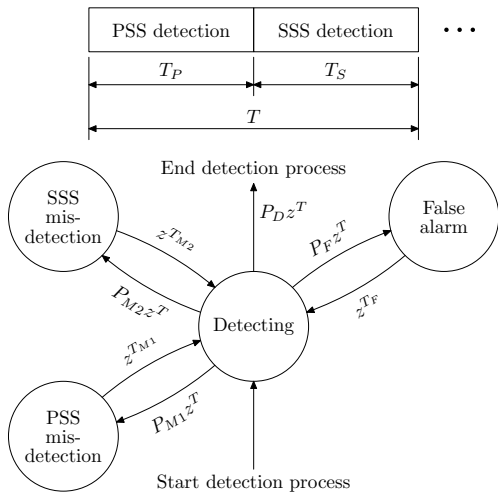

Fig. 9. Single dwell cell search process and corresponding state diagram.

D. Cell-Search Time and Computing Power Analyses

The cell-search time and the corresponding battery consumption of the proposed cell-search scheme are the most important considerations to achieve long battery life for low-power IoT devices. The cell-search time not only indicates the performance of PSS and SSS detectors but also helps in deciding system parameters such as detection thresholds as shown in Subsection V-B. We analyze the average and the standard deviation of cell-search time using a Markovian

model for single-dwell detection procedure [33], [46], [47]. In the procedure, the single dwell time is $T = T_P + T_S$, where $T_P = T_S = W_p/(\eta N)$ are the time durations for the PSS and SSS detectors, respectively. The state diagram plotted in Fig. 9 illustrates a cell detection process and the corresponding state diagram. The values on the outgoing branches from the Detecting state to each of the PSS mis-detection, SSS mis-detection, and False alarm states indicate the probabilities of each transition, multiplied by a power of the dummy variable z used to determine the transfer function of the state diagram. The power is utilized to indicate the hypothesis testing time periods needed to make the given transition [47]. In Fig. 9, P_D, P_{M1}, P_{M2}, and P_F are the detection, PSS mis-detection, SSS mis-detection, and false alarm probabilities, respectively, which are defined as: $P_D = \Pr\{$Both detections are correct, $D_1 \geq T_1$ and $D_2 \geq T_2\}$; $P_{M1} = \Pr\{D_1 < T_1\}$; $P_{M2} = \Pr\{D_2 < T_2\}$; and $P_F = \Pr\{$One of PSS and SSS detection is incorrect, but $D_1 \geq T_1$ and $D_2 \geq T_2\}$.

Note that correct PSS and SSS detections are defined in Subsections V-A1 and V-B, respectively, $P_D + P_{M1} + P_{M2} + P_F = 1$, T_F is the false alarm time, T_{M1} is the time to perform a PSS mis-detection, and T_{M2} is the time to perform an SSS mis-detection. T_F is set to be $10W_p/(\eta N)$ in order to consider the processing delay caused by decoding the information related to accessing the system. T_{M1} and T_{M2} are set to $W_p/(\eta N)$ and $2W_p/(\eta N)$, respectively, on the assumption that the SSS detection is performed within the next window size just after obtaining the starting sample time of the CP-excluded SSS TD signal obtained by the PSS detection. From the state diagram in Fig. 9, its transfer function is formulated as

$$U(z) = \frac{P_D z^T}{1 - P_{M1} z^T z^{T_{M1}} - P_{M2} z^T z^{T_{M2}} - P_F z^T z^{T_F}}. \quad (26)$$

Given $U(z)$, the average cell-search time is expressed as

$$T_{avg} = \frac{dU(z)}{dz}\bigg|_{z=1} = \frac{\Upsilon}{P_D}, \quad (27)$$

where $\Upsilon = T + T_{M1} P_{M1} + T_{M2} P_{M2} + T_F P_F$. Given T_{avg}, the standard deviation T_{std} of cell-search time is expressed as, with $\Gamma = (T_{M1})^2 P_{M1} + (T_{M2})^2 P_{M2} + (T_F)^2 P_F$,

$$T_{std} = \sqrt{\left[\frac{d^2 U(z)}{dz^2}\right]_{z=1} + T_{avg}\left(1 - T_{avg}\right)} \quad (28)$$

$$= \sqrt{\frac{\Upsilon^2}{(P_D)^2} + \frac{\Gamma - T^2}{P_D}}.$$

It is intractable to derive the absolute battery consumption of the scheme. Instead, it is possible to compare the relative battery consumption under the assumption that the battery consumption is linearly proportional to average computing power $\wp_{avg}$ (i.e., average number of operations) to perform cell search. This computing power can be obtained from the same state diagram in Fig. 9, where each state corresponds to the computing power of the event, expressed as

$$\wp_{avg} = \frac{(\$_p + \$_s)T + \$_p T_{M1} P_{M1} + \$_s T_{M2} P_{M2} + \$_f T_F P_F}{P_D},$$

where the computing power $\$_f$ to perform false alarm process is assumed to be identical to $\$_p + \$_s$ as one of examples. Here,

the computing powers of PSS and SSS are represented in units of MOPS, which are derived in Tables. V and VI.

V. Performance Evaluation

The performances of the proposed cell-search schemes are evaluated with the parameter settings listed in Table VII. Two branch Rx equal gain combining diversity (i.e., $a = 0, 1$ in (3)) with no Tx diversity is assumed. 3GPP Tapped Delay Line A (TDL-A) channel for non-line-of-sight (NLoS) and TDL-D channel for line-of-sight (LoS) in [48] are adopted as the channel models. A two-cell model comprising a serving cell c and a dominant interfering cell c' such that $c' \neq c$ is employed where two cells are configured with different PIDs and PCIs. The signal arrival time difference of the adjacent cell relative to the serving cell is assumed to be uniformly distributed within half of CP duration, i.e., $[-0.5\lfloor N_{cp}^6/(\eta N)\rfloor, 0.5\lfloor N_{cp}^6/(\eta N)\rfloor]$. The average Rx power of the serving cell P_s^c is set to 9 dB larger than $P_s^{c'}$. Moreover, all of the feasible subcarriers corresponding to other channels are always loaded (i.e., full system load), and the same transmission power is allocated to each of the used subcarriers in the SS block and those in all of the OFDM symbols except for the SS block in Fig. 1.

TABLE VII
EVALUATION PARAMETERS.

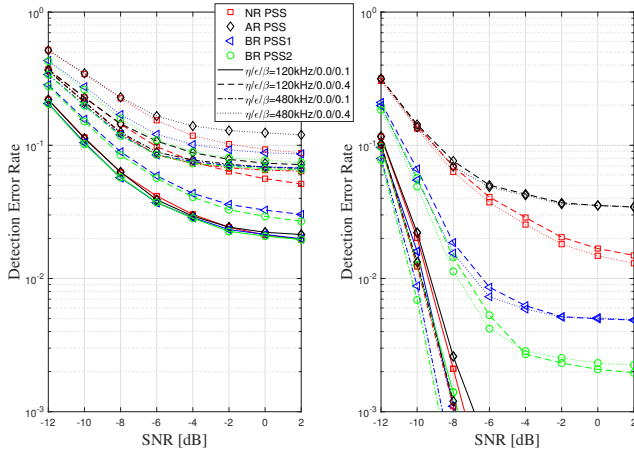| Parameter	Value
Carrier frequency	70 GHz
Normalized CFO ϵ	0 / 0.67
Normalized PhN linewidth β	0.0 / 0.1 / 0.4
RMS delay spread	16 ns
MS velocity	3 km/h
SCS η	120 kHz / 480 kHz
FFT size N	256

Fig. 10. PSS DER vs. SNR per Rx antenna with TDL-A (Left) and TDL-D (Right) in the presence of $\beta = 0.1$ and 0.4 only.

A. Evaluation for PSS Detection

The performance of PSS detection can be evaluated by two metrics: detection error rate (DER) and root mean squared error (RMSE) of sample time estimate.
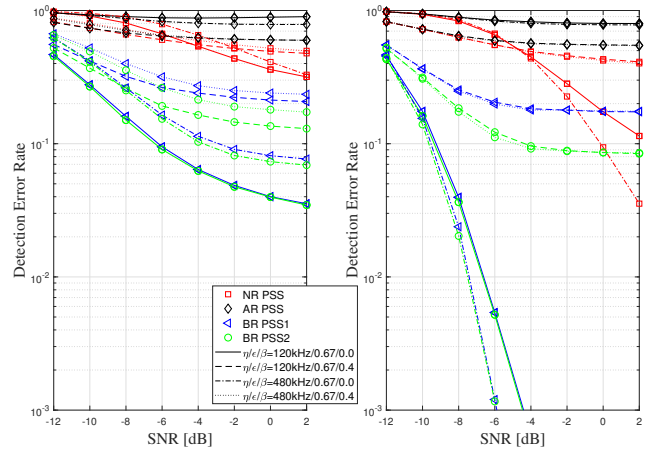
Fig. 11. PSS DER vs. SNR per Rx antenna with TDL-A (Left) and TDL-D (Right) in the presence of $\epsilon = 0.67$ and $\beta = 0.0$ and 0.4.

*1) **PSS DER**:* The timing accuracy performance in the PSS detection is evaluated with the DER as follows: if the detected sample time is within the one-sixteenth of absolute CP (i.e., decision bound corresponding to ±1 sample points close to perfect synchronization), and the detected PID belongs to the serving cell or the adjacent cell, a successful detection is declared; otherwise, an error is declared. This DER is the most important performance measure in a factory automation that requires a certain timing accuracy with high reliability because the DER is regarded as an outage probability that an absolute value of detected STO exceeds a required absolute value of STO.[4]

Figs. 10 and 11 show the DER performances as a function of SNR per Rx antenna with the PSS detection threshold $T_1 = 0$ whose optimal value will be analyzed in Subsection V-C. BR PSSs outperform in terms of DER in all cases of HW impairments, SCSs, and wireless channel models. Due to the effect of frequency selectivity, all DER performances in the TDL-A with more frequency selectivity are worse than those in the TDL-D with a strong direct path. AR PSS provides the worst DER performance in the decision bound of 1/16 CP, which may result from the high sidelobes existing out of the bound. However, AR PSS outperformed NR PSS in terms of DER in the decision bound of 1/2 CP employed in [33] thanks to the sidelobes mainly existing within this loose bound. This implies that a timing detection performance (e.g., DER) depends on the decision bound. So does cell-search performance, which is observed in Subsection V-C. In the case of TDL-A, as SCS η increases, DER becomes higher because $\eta = 480$ kHz causes more frequency selectivity over $\eta = 120$ kHz. In the case of TDL-D, as SCS η increases, DER becomes lower owing to the shorter OFDM symbol duration under the less frequency selectivity.

In Fig. 10 in the presence of PhN only without CFO, the following observations are made. In both case of TDL-A and TDL-D, there are not much DER differences among PSS signals in the lower PhN linewidth of $\beta = 0.1$; BR PSSs

---

[4]Note that the robustness of BR PSSs against high HW impairments compared to NR PSS and AR PSS can be observed by DER in a sense that the more robust against HW impairments, the more precise timing accuracy.

provide an SNR gain of more than 2 dB over NR PSS and AR PSS. As the received SNR increases, the gap of SNR gain becomes higher. In Fig. 11 in the presence of high CFO with/without PhN, BR PSS1 and PSS2 are the most robust against CFO to the same extent. On the contrary, NR PSS and AR PSS are very weaker in terms of CFO. BR PSSs provide an SNR gain of more than 15 dB over NR PSS. While there is not much DER difference between BR PSS1 and PSS2 in the absence of PhN, BR PSS2 outperforms BR PSS1 in terms of DER in the mixture of CFO and PhN. Summing up all observations, it can be elucidated that the most effective PSS that can reduce timing detection complexity while being robust against HW impairments is BR PSS2.
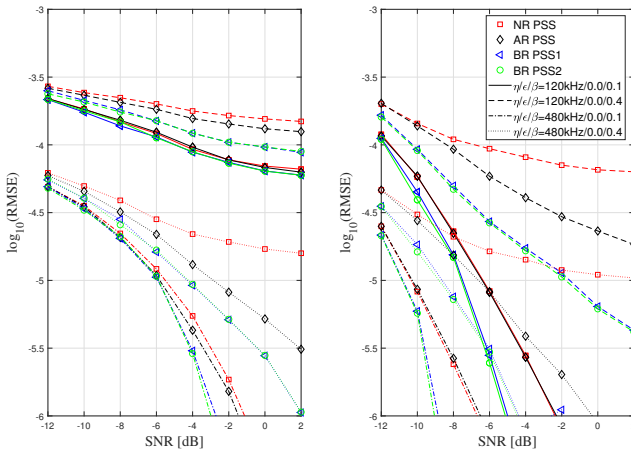

Fig. 12. PSS $\log_{10}$(RMSE) vs. SNR per Rx antenna with TDL-A (Left) and TDL-D (Right) in the presence of $\beta = 0.1$ and 0.4 only.
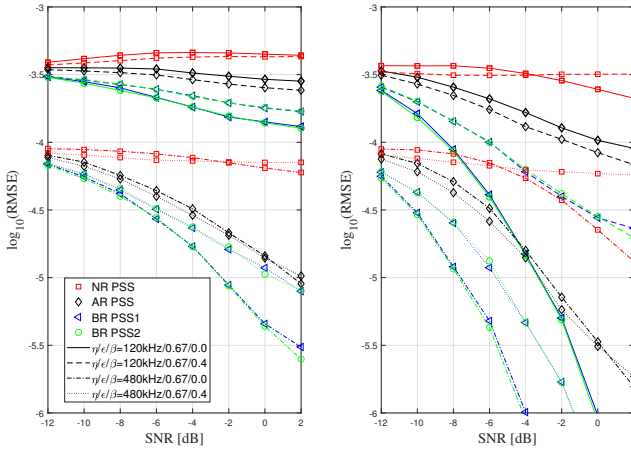

Fig. 13. PSS $\log_{10}$(RMSE) vs. SNR per Rx antenna with TDL-A (Left) and TDL-D (Right) in the presence of $\epsilon = 0.67$ and $\beta = 0.0$ and 0.4.

2) PSS RMSE: As a widely adopted metric, the timing accuracy performance in the PSS detection is evaluated with the RMSE of detected sample time. Figs. 12 and 13 show the RMSE performances as a function of SNR per Rx antenna. The results show that the tendency of RMSE performances is almost consistent with that of the DER performances as shown in Figs. 10 and 11. The two notable differences between the DER and RMSE results are observed as follows. Firstly, in terms of RMSE, the PSS signals with the higher SCS of

$\eta = 480$ kHz provide lower RMSE than those with the lower SCS of $\eta = 120$ kHz because the time duration of PSS of the higher SCS is shorter than that of the lower SCS. AR PSS provides lower RMSE than NR PSS because there are less sample time estimates that deviate excessively beyond CP than NR PSS, while AR PSS has higher sidelobes around CP at performing timing detection.

B. Evaluation for SSS Detection

SSS detection performance is evaluated with DER as follows: if the detected PCI belongs to the serving cell or the adjacent cell (i.e., the detected PCI is correct), a successful detection is declared; otherwise, an error is declared. Fig. 14 compares DER performances with SCS $\eta = 120$ kHz and 480 kHz in 3GPP TDL-A and TDL-D channel, respectively. For SSS performance evaluation, unnormalized residual CFO $\tilde{\epsilon}$ after PSS detection is assumed to be 7 kHz (i.e., 0.1 ppm), and PhN linewidth β is set as 0.1 and 0.4. SSS detection threshold T_2 is set to 0, and the optimal value of T_2 will be provided in Subsection V-B together with PSS detection threshold T_1.
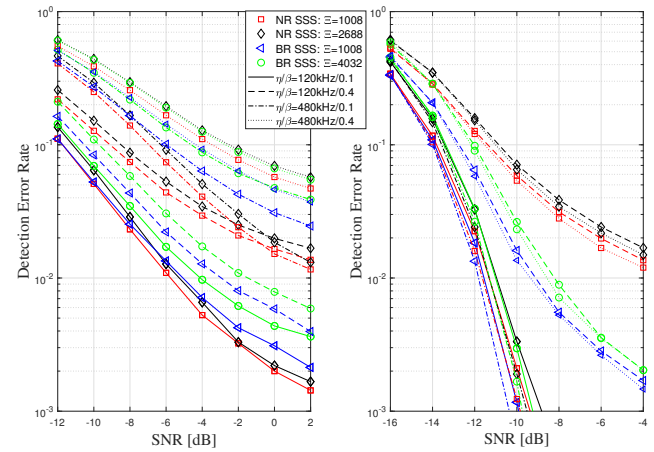

Fig. 14. SSS DER vs. SNR per Rx antenna with TDL-A (Left) and TDL-D (Right).

In Fig. 14, an increase of number of PCIs Ξ causes SNR shift in both NR and BR SSS because the number of PCI hypotheses close to the peak cross-correlation output increases. DER of NR SSS with $\Xi = 2688$ is shifted by SNR= 0.35 to 2 dB compared to NR SSS with baseline $\Xi = 1008$ under various SCS η and PhN linewidth β. DER of BR SSS with $\Xi = 4032$ is shifted by SNR= 0.5 to 3 dB compared to BR SSS with baseline $\Xi = 1008$. It can be observed that the amount of SNR shift generally increases as the phase distortion caused by frequency selectivity and PhN deteriorates.

In TDL-D channel, first, BR SSS with baseline $\Xi = 1008$ achieves lower DER than NR SSS with baseline $\Xi = 1008$ at the same parameters of η and β. In particular, BR SSS has steeper DER slopes than NR SSS in the high SNR regime, which implies that BR SSS captures higher diversity order than NR SSS in the high PhN environment. The difference of the DER slope between BR and NR SSS increases as β increases. BR SSS with $\eta = 480$ kHz achieves DER about 10^{-2} at SNR= -10 dB shifted by -6 dB relative to NR SSS with $\eta = 480$ kHz for $\beta = 0.4$. Second, PhN environment with

$\eta = 120$ kHz and $\beta = 0.4$ has the same level of single-sided power spectral density as the environment with $\eta = 480$ kHz and $\beta = 0.1$. The DER performances of both BR and NR SSS with $\eta = 480$ kHz greatly improve in the high SNR regime owing to the reduction of ICI.

Both BR and NR SSS provide higher DER in TDL-A than in TDL-D because they suffer frequency selectivity despite short delay spread due to wide SCS. NR SSS with $\eta = 120$ kHz has the lowest DER in TDL-A channel for $\beta = 0.1$ where the frequency selectivity dominantly affects the sequence property than PhN. However, for $\beta = 0.4$ where PhN dominantly impinges on the sequence property, BR SSS provides lower DER than NR SSS, which is robust to ICI. On the other hand, when NR SSS for $\eta = 120$ kHz, $\beta = 0.4$ is compared with for $\eta = 480$ kHz, $\beta = 0.1$, NR SSS with wider SCS provides higher DER at low SNR but lower DER at high SNR. There exists a tradeoff between the reduction of ICI and increased frequency selectivity for the non-coherent detection method. However, BR SSS always achieves better DER performance for lower SCS owing to the robustness against HW impairments. In sum, BR SSS with $\eta = 120$ kHz shows the lowest DER compared to the counterparts in the frequency-selective channel with high PhN. BR SSS with $\Xi = 1008$ and $\Xi = 4032$ achieves DER about 10^{-2} at SNR$= -4$ and -2 dB, respectively, whereas NR SSS with $\Xi = 1008$ provides same the DER at SNR$= 2$ dB.
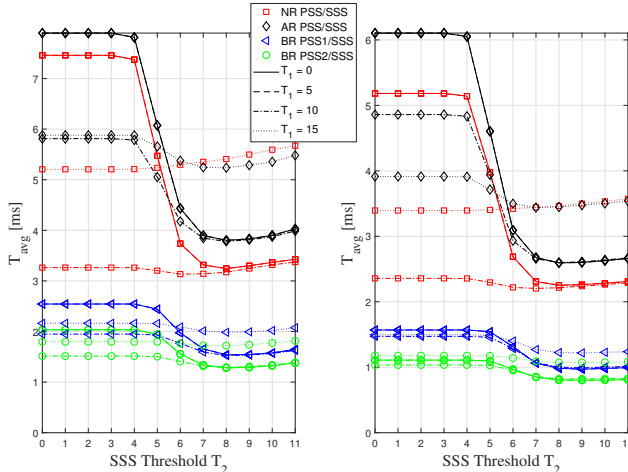

Fig. 15. Cell-search time T_{avg} vs. SSS threshold T_2 at SNR $= -6$ dB and $\eta = 480$ kHz with TDL-A (Left) and TDL-D (Right).

C. Cell-Search Time and Computing Power

TABLE VIII
COMPARISON ON THE LOWEST CELL-SEARCH TIME.

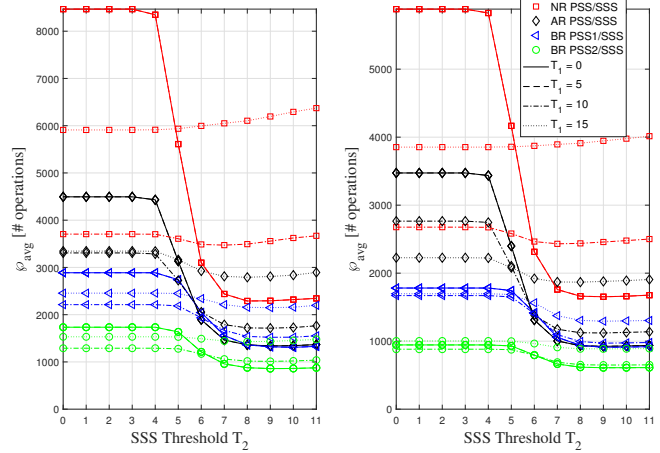| BR PSS1/SSS	BR PSS2/SSS	AR PSS/SSS	NR PSS/SSS
Lowest T_{avg} [ms] / T_{std} [ms] at $\eta = 120$ kHz & TDL-A			
5.11 / 4.64	4.29 / 3.64	13.28 / 13.05	10.73 / 10.17
Lowest T_{avg} [ms] / T_{std} [ms] at $\eta = 120$ kHz & TDL-D			
4.00 / 3.39	3.29 / 2.31	10.57 / 10.17	8.74 / 7.98
Lowest T_{avg} [ms] / T_{std} [ms] at $\eta = 480$ kHz & TDL-A			
1.52 / 1.49	1.29 / 1.20	3.78 / 3.76	3.13 / 3.02
Lowest T_{avg} [ms] / T_{std} [ms] at $\eta = 480$ kHz & TDL-D			
0.97 / 0.83	0.81 / 0.54	2.60 / 2.50	2.20 / 2.00

Fig. 16. Computing power $\wp_{avg}$ vs. SSS threshold T_2 at SNR $= -6$ dB and $\eta = 480$ kHz with TDL-A (Left) and TDL-D (Right).

Fig. 15 shows cell-search time performances where P_D, P_{M1}, P_{M2}, and P_F are obtained through the evaluations at SNR $= -6$ dB and SCS $\eta = 480$ kHz according to various PSS detection threshold T_1 and SSS detection threshold T_2. The evaluations are performed under CFO $\epsilon = 0.67$ and PhN linewidth $\beta = 0.4$, and the evaluations at $\eta = 120$ kHz are omitted that show similar trend with those at $\eta = 480$ kHz. The proposed schemes BR PSS2/SSS and PSS1/SSS outperform existing NR PSS/SSS and AR PSS/SSS in terms of average cell-search time T_{avg}, which implies the proposed schemes show superior robustness to high CFO/PhN over NR and AR. Specifically, in $0.0 \leq T_2 \leq 4.0$, each T_{avg} of BR, AR, and NR is almost constant regardless of the value of T_1. Since a tight decision bound on timing detection is employed, AR provides worse cell-search time performance over NR owing to the sidelobe effect. Although there are slight differences depending on the SSS threshold in $T_2 > 7.0$, lower T_1 reduces T_{avg}, and BR PSS2/SSS provides around 60 % lower average cell-search time over NR PSS/SSS. The results indicate that an effective cell search with BR can be achieved by only setting $T_2 = 8.0$ without any PSS detection thresholds (i.e., $T_1 = 0.0$). Table VIII shows the lowest average and standard deviation of cell-search time of each cell-search scheme according to different SCS η and wireless channel. The proposed schemes outperform AR and NR in terms of T_{avg} and T_{std} due to the robustness against CFO/PhN, where BR PSS2/SSS provides a slightly lower T_{avg} and T_{std} compared to BR PSS1/SSS.

Fig. 16 shows average computing powers $\wp_{avg}$ to perform cell search for the same parameters as Fig. 15. The proposed BR PSS2/SSS provides about 80 % lower computing power compared to NR PSS/SSS. AR PSS/SSS provides almost identical computing power to BR PSS1/SSS at the minimum value of T_{avg} (for $T_1 = 0.0$ and $T_2 = 8.0$) thanks to the lowest PSS detection complexity. To sum up, BR PSS2/SSS shows the lowest value of average and standard deviation of cell-search time and computing power under the harsh HW impairments, effectively reducing the battery consumption.

VI. CONCLUSION

This work has proposed synchronization signals for cell search in over-6GHz wireless time-critical industrial IoT sys-

tems. The distributed concatenation of a base sequence and its modification in the proposed PSS and SSS greatly improves the robustness to HW impairments such as CFO and PhN in the time and frequency domain, respectively. Under the harsh HW impairments, specifically, the proposed PSS signal has provided lower computational complexity by exploiting the symmetry of ZC sequence at the same time providing up to 15 dB SNR gain in terms of timing detection performance than NR PSS. The proposed SSS signal that is constructed by BPSK-modulated Kasami sequence has provided 1.5 times more distinguishable cell IDs while achieving up to 6 dB SNR gain in cell ID detection performance over NR SSS. It has been indicated that shorter cell-search time or lower battery consumption can be attained by only setting an SSS threshold. The proposed cell-search scheme with the optimal thresholds offers about 60 % shorter cell-search time and about 80 % lower battery consumption than NR cell-search scheme under the severe HW impairments, eventually increasing the battery life of wireless low-power IoT devices. Not only the effect of other HW impairments such as DC offset or I-Q imbalance on cell-search performance but also theoretical timing and PCI detection probabilities are to be further studied.

APPENDIX

A. Proof of Proposition 1

Let

$$b_u(n) = e^{-j\pi un(n+1)/M} \tag{29}$$

be a Zadoff-Chu sequence where

$$M = \text{length of the sequence, odd;}$$
$$n = 0, 1, \cdots, M - 1;$$
$$u = 0, 1, \cdots, M - 1.$$

Then, it is straightforward to show that $b_u(n)$ is symmetric with respect to $n = (M - 1)/2$ (called *the symmetry of ZC*). That is,

$$b_u(M - 1 - m) = b_u(m) \tag{30}$$

for $m = 0, 1, \cdots, M - 1$.

Let $\mathbf{f}$ be an $(N \times 1)$ IDFT vector as illustrated in Fig. 17, where N is a power of 2. Then, $\mathbf{f}$ exhibits different periodic properties for different values of n.

$k = 0$	1
$k = 1$	$\exp(j2\pi n/N)$
$\vdots$	$\vdots$
$k = N - 2$	$\exp(j2\pi(N-1)n/N)$
$k = N - 1$	$\exp(j2\pi(N-1)n/N)$

Fig. 17. $(N \times 1)$ IDFT vector $\mathbf{f}$.

Fig. 18 illustrates the periodic properties of $\mathbf{f}$ for various values of n. For example, when $n = 1$, the first half of $\mathbf{f}$ (indicated as "A") and the second half of $\mathbf{f}$ (indicated as "$-A$") are identical to each other except for the negative sign. Similarly, when $n = 2$, the the first quarter ("B") and the second quarter ("$-B$") of $\mathbf{f}$ are identical to each other

except for the negative sign. The second half of $\mathbf{f}$ is simply a repetition of an exact copy of the first half of $\mathbf{f}$. The IDFT vector $\mathbf{f}$ displays similar periodic pattern with higher number of repetitions as n increases (called *the periodicity of IDFT*).
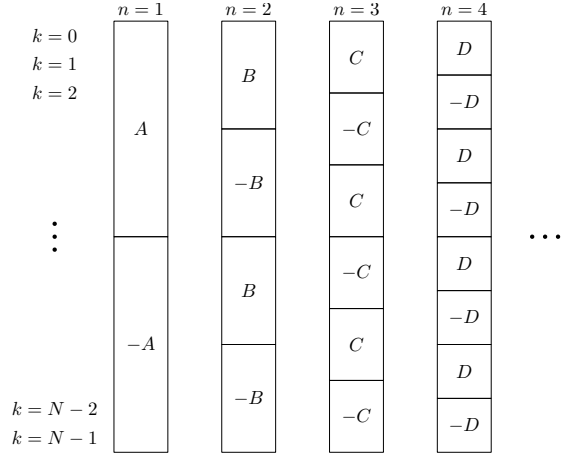

Fig. 18. Periodic structure of IDFT vector $\mathbf{f}$.

Fig. 19 shows the proposed PSS2 signal in frequency domain. Let $X(k)$, $k = 0, 1, \cdots, N - 1$, be the frequency-domain samples of PSS2, then

$$x(n) = \frac{1}{N} \sum_{k=0}^{N-1} X(k) e^{j\frac{2\pi nk}{N}}, \quad n = 0, 1, \cdots, N - 1. \tag{31}$$

Since $X(k) = 0$ for $M < k < N - M - 1$ and the periodicity of IDFT as shown in Fig. 18, (31) can be written as

$$x(n) = \frac{1}{N} \sum_{k=0}^{M} X(k) e^{j\frac{2\pi nk}{N}} + \frac{1}{N} \sum_{k=N-M-1}^{N-1} X(k) e^{j\frac{2\pi nk}{N}}. \tag{32}$$

Note that, because of the symmetry of ZC shown in (30) and the concatenation rule of PSS2 described in (9),

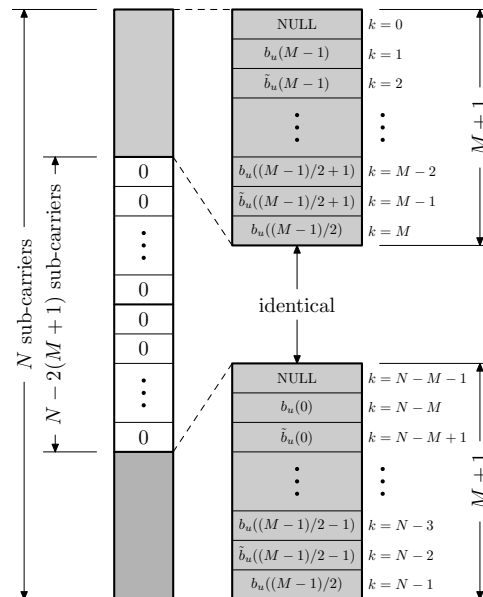$$X(k) = X(k + (N - M - 1)), \quad k = 0, 1, \cdots, M. \tag{33}$$

Fig. 19. Illustration of the IDFT input of PSS2 in frequency domain.

From (32) and (33),

$$x(n) = \frac{1}{N}\sum_{k=0}^{M} X(k) e^{j\frac{2\pi nk}{N}} + \frac{1}{N}\sum_{m=0}^{M} X(m+N-M-1) e^{j\frac{2\pi n(m+N-M-1)}{N}}$$

$$= \left(1 + e^{j\frac{2\pi n(N-M-1)}{N}}\right)\frac{1}{N}\sum_{k=0}^{M} X(k) \cdot e^{j\frac{2\pi nk}{N}}$$

$$= \left(1 + e^{-j\frac{2\pi n(M+1)}{N}}\right)\frac{1}{N}\sum_{k=0}^{M} X(k) \cdot e^{j\frac{2\pi nk}{N}}. \tag{34}$$

Note that $x(n) = 0$ when $2n(M+1)/N$ is an odd integer. That is, $2n(M+1)/N = \pm(2\alpha - 1), \ \alpha = 1, 2, \cdots$. Since $n \geq 0$, this implies that $x_n = 0$ when

$$n = (2\alpha - 1)\frac{N}{2(M+1)}, \quad \alpha = 1, 2, \cdots.$$

B. Proof of Proposition 2

Let the IDFT output $x(n)$ $(n = 0, 1, ..., N-1)$ of input elements $X(k)$ $(k = 0, 1, ..., N-1)$ be expressed as

$$x(n) = \frac{1}{N}\sum_{k=0}^{N-1} X(k) e^{j\frac{2\pi nk}{N}} \tag{35}$$

$$= \underbrace{\frac{1}{N}\sum_{m=0}^{\frac{N}{2}-1} X(2m) e^{j\frac{2\pi n(2m)}{N}}}_{x_1(n)} + \underbrace{\frac{1}{N}\sum_{m=0}^{\frac{N}{2}-1} X(2m+1) e^{j\frac{2\pi n(2m+1)}{N}}}_{x_2(n)}$$

$$= x_1(n) + \underbrace{e^{j\frac{2\pi n}{N}}\frac{1}{N}\sum_{m=0}^{\frac{N}{2}-1} X(2m+1) e^{j\frac{2\pi n(2m)}{N}}}_{x_2(n)}.$$

Regarding BR PSS1, $X(2m+1) = -X((M-2) - 2m)$ as shown in (8) and Fig. 3(a). Applying the symmetry of ZC (30) to odd IDFT input elements, $X((M-2) - 2m) = X(2m)$ so that exactly $X(2m+1) = -X(2m)$ for $m = 0, 1, ..., N/2 - 1$. Using the property of IDFT output for even input elements with zero-padded odd input elements [40],

$$x_{2,\text{pss1}}(n) = \begin{cases} -x_{1,\text{pss1}}(n) e^{j\frac{2\pi n}{N}}, & 0 \leq n < \frac{N}{2} \\ -x_{1,\text{pss1}}([n]_{N/2}) e^{j\frac{2\pi [n]_{N/2}}{N}}, & \frac{N}{2} \leq n < N. \end{cases} \tag{36}$$

Regarding BR PSS2, since $X(2m+1) = -X(2m)$ for $m = 1, 2, ..., N/2 - 1$ without $m = 0$ as shown in (9) and Fig. 3(b), $x_2(n) = -\exp\{j2\pi n/N\}x_1(n)$ in (35). Using the property used in (36),

$$x_{2,\text{pss2}}(n) \approx \begin{cases} -x_{1,\text{pss2}}(n) e^{j\frac{2\pi n}{N}}, & 0 \leq n < \frac{N}{2} \\ -x_{1,\text{pss2}}([n]_{N/2}) e^{j\frac{2\pi [n]_{N/2}}{N}}, & \frac{N}{2} \leq n < N \end{cases}$$

where an exact equivalence is not established because $P_u(M) = 0$ (i.e., $X(0) = 0$) in Fig. 3(b) to realize the periodical zero as proved in Appendix A.

REFERENCES

[1] *Internet of Things (IoT) Market Size, Share & COVID-19 Impact Analysis, by Component (Platform, Solution & Services), by End-Use Industry (BFSI, Retail, Government, Healthcare, Manufacturing, Agriculture, Sustainable Energy, Transportation, IT & Telecom, Others), and Regional Forecast, 2021-2029*, Fortune Business Insights, 2021.

[2] E. Dahlman, S. Parkvall, J. Skold, *5G NR: The next generation wireless access technology.* Academic Press, 2018.

[3] *Smart Manufacturing and How to Get Started: The Implementation and ROI of Industry 4.0 use cases*, ABI Research, May 2020.

[4] IEEE 1588-2019 (PTP v2.1), *White Rabbit (WR)*, Accessed: Jun. 16, 2019. [Online]. Available: https://standards.ieee.org/standard/1588-2019.html

[5] N. H. Mahmood et al., "Machine type communications: Key drivers and enablers towards the 6G era," *Eurasip J. Wirel. Commun. N.,* Open Access, Jun. 2021.

[6] X. Lin, "An overview of 5G advanced evolution in 3GPP Release 18," *arXiv preprint arXiv:* 2201.01358, 2022.

[7] C. D. Lima et al., "Convergent communication, sensing and localization in 6G systems: an overview of technologies, opportunities and challenges," *IEEE Access*, vol. 9, pp.26902-26925, Jan. 2021.

[8] H. Wymeersch et al., "Integration of communication and sensing in 6G: A joint industrial and academic perspective," in *Proc. IEEE PIMRC*, 2021.

[9] TS36.211 v13.5.0, "Physical channels and modulation (Release 13)," *3GPP TSG RAN*, pp. 125-128, Mar. 2017.

[10] TS36.213 v13.6.0, "Physical layer procedures (Release 13)," *3GPP TSG RAN,* June 2017.

[11] S. Sesia, I. Toufik, and M. Baker, *LTE - The UMTS Long Term Evolution: From Theory to Practice,* New York: John Wiley & Sons, 2009.

[12] TS38.211 v17.1.0, "NR; Physical channels and modulation (Release 17)," *3GPP TSG RAN*, Mar. 2022.

[13] TS38.101-2 v17.6.0, "NR; User equipment (UE) radio transmission and reception; Part 2: Range 2 Standalone (Release 17)," *3GPP TSG RAN*, Jun. 2022.

[14] B. Razavi, *RF microelectronics*, Prentice Hall, 2nd Edition, 2012.

[15] A. Mohammadian and C. Tellambura, "RF impairments in wireless transceivers: Phase Noise, CFO, and IQ imbalance - A survey," *IEEE Access*, vol. 9, pp. 111718-111791, 2021.

[16] X. Li, J. Li, Y. Liu, Z. Ding, and A. Nallanathan, "Residual transceiver hardware impairments on cooperative NOMA networks," *IEEE Trans. Wireless Commun.*, vol. 19, no. 1, pp. 680-695, Jan. 2020.

[17] Ericsson, "On phase noise compensation for OFDM," *3GPP TSG RAN WG1*, Tdoc R1-2005922, Meeting #102-e, Aug. 2020.

[18] 5G Alliance for Connected Industries and Automation, "5G for Connected Industries and Automation," *White Paper*, 2nd edition, Feb. 2019.

[19] J. L. Volakis, *Antenna Engineering Handbook*, 4th edition, (pp. 700-720) New York, NY, USA: McGraw-Hill Education, 2007.

[20] M. M. Mansour, "Optimized architecture for computing Zadoff-Chu sequences with application to LTE," in *Proc. IEEE Globecom*, 2009.

[21] W. Xu and K. Manolakis, "Robust synchronization for 3GPP LTE systems," in *Proc. IEEE Globecom,* Miami, FL, 2010.

[22] Z. Zhang, K. Long, and Y. Liu, "Complex efficient carrier frequency offset estimation algorithm in OFDM systems," *IEEE Trans. Broadcast.,* vol. 50, no. 2, pp. 159-164, Jun. 2004.

[23] J. Yuan and M. Torlak, "Joint CFO and SFO estimator for OFDM receiver using common reference frequency," *IEEE Trans. Broadcast.*, vol. 62, no. 1, pp. 141-149, Mar. 2016.

[24] M. Morelli and M. Moretti, "A robust maximum likelihood scheme for PSS detection and integer frequency offset recovery in LTE systems," *IEEE Trans. Wireless Commun.*, vol. 15, no. 2, pp. 1353-1363, 2016.

[25] J.-C. Lin, Y.-T. Sun, and H. V. Poor, "Initial synchronization exploiting inherent diversity for the LTE sector search process," *IEEE Trans. Wireless Commun.*, vol. 15, no. 2, pp. 1114-1128, Feb. 2016.

[26] C. Hu and Y. Zhang, " 5G NR primary synchronization signal detection with low hardware resource occupancy," in *Proc. IEEE ICCC,* pp. 304-308, 2018.

[27] H. Abdzadeh-Ziabari, W.-P. Zhu, and M. N. S. Swamy, "Joint maximum likelihood timing, frequency offset, and doubly selective channel estimation for OFDM systems," *IEEE Trans. Veh. Technol.*, vol. 67, no. 3, pp. 2787-2791, Mar. 2018.

[28] R. Zeng, H. Huang, L. Yang, and Z. Zhang, "Joint estimation of frequency offset and Doppler shift in high mobility environments based on orthogonal angle domain subspace projection," *IEEE Trans. Veh. Technol.,* vol. 67, no. 3, pp. 2254-2266, Mar. 2018.

[29] A. Omri, M. Shaqfeh, A. Ali, and H. Alnuweiri, "Synchronization procedure in 5G NR systems," *IEEE Access,* pp. 41286-41295, 2019.

[30] K. Chang and Y. Han, "Robust replica correlation-based symbol synchronization in OFDM systems," *Electronics Letters,* vol. 44, no. 17, pp. 1024-1025, Aug. 2008.

[31] K. Chang, P. Ho, and Y. Choi, "Signal design for reduced-complexity and accurate cell search/synchronization in OFDM-based cellular systems," *IEEE Trans. Veh. Technol.*, vol. 61, no. 9, pp. 4170-4174, Nov. 2012.

[32] M.M.U. Gul, X. Ma, and S. Lee, "Timing and frequency synchronization for OFDM downlink transmissions using Zadoff-chu sequences," *IEEE Trans. Wireless Commun.*, vol. 14, no. 3, pp. 1716-1729, Mar. 2015.

[33] K. Chang and S. Lee, "Robust OFDM-based synchronization against very high fractional CFO and time-varying fading," *IEEE Systems Journal,* vol. 14, no. 3, pp. 4047-4058, Sept. 2020.

[34] P. Wang and F. Berggren, "Secondary synchronization signal in 5G New Radio," in *Proc. IEEE ICC,* May 2018.

[35] A. Mahmood, M. I. Ashraf, M. Gidlund, and J. Torsner, "Over-the-air time synchronization for URLLC: Requirements, challenges and possible enablers," in *Proc. IEEE ISWCS,* 2018.

[36] A. Mahmood, M. I. Ashraf, M. Gidlund, J. Torsner, and J. Sachs, "Time synchronization in 5G wireless edge: Requirements and solutions for critical MTC," *IEEE Commun. Mag.*, pp. 45-51, Dec. 2019.

[37] S. Wu and Y. Bar-Ness, "OFDM systems in the presence of phase noise: Consequences and solutions," *IEEE Trans. Commun.*, pp. 1988-1996, 2004.

[38] M. Chung, L. Liu, and O. Edfors, "Phase-noise compensation for OFDM systems exploiting coherence bandwidth: Modeling, algorithms, and analysis," *IEEE Trans. Wireless Commun.*, vol. 21, no. 5, pp. 3040-3056, May 2022.

[39] M. Speth, F. Classen, and H. Meyr, "Frame synchronization of OFDM systems in frequency selective fading channels," in *Proc. IEEE VTC,* vol. 3, 1997.

[40] S. Glisic, *Advanced wireless communications: 4G technologies,* John Wiley & SONS, 2004.

[41] J. J. van de Beek, M. Sandell, P. O. Börjesson, "ML estimation of time and frequency offset in OFDM systems," *IEEE Trans. Signal Processing,* vol. 45, no. 7, pp. 1800-1805, Jul. 1997.

[42] H. Meyr, M. Moeneclaey, and S. A. Fechtel, *Digital communication receivers: Synchronization, channel estimation, and signal processing,* John Wiley & SONS, Oct. 2001.

[43] I. Kim, Y. Han, and H. K. Chung, "An efficient synchronization signal structure for OFDM-based cellular systems," *IEEE Trans. Wireless Commun.,* vol. 9, no. 1, pp. 99-105, Jan. 2010.

[44] Intel, "On device complexity for NB-IoT cell search," *3GPP TSG RAN WG1*, Tdoc R1-155853, Meeting #82bis, Sweden, October 2015.

[45] M. Cohn and A. Lempel, "On fast M-sequence transforms (Corresp.)," *IEEE Trans. Inf. Theory*, vol. 23, no. 1, pp. 135-137, Jan. 1977.

[46] A. Polydoros and C. L. Weber, "A unified approach to serial search spread spectrum acquisition-Part I: General theory," *IEEE Trans. Commun.,* vol. 32, pp. 542-549, May 1988.

[47] A. J. Viterbi, *CDMA: Principles of Spread Spectrum Communications,* Reading, MA: Addison-Wesley, ch. 3, 1995.

[48] 3GPP TR38.901 v16.1.0, "Study on channel model for frequencies from 0.5 to 100 GHz," Jan. 2020.